

Sodium disrupts mitochondrial energy metabolism to execute NECSO

Received: 1 November 2024

Accepted: 25 November 2025

Published online: 13 December 2025

Yuhui Qiao^{1,2}, Jianghuang Wang², Bohong Wang^{3,4}, Hong Zhou², Qianlin Ni^{3,4}, Wan Fu²✉, Zeping Hu^{3,4}✉ & Qing Zhong²✉

Na⁺ influx is a critical pathological event in various conditions such as ischemia, hyperosmotic stress, and organ failure. Although persistent activation of the transient receptor potential cation channel subfamily M member 4 (TRPM4) by chemical agonist Necroside 1 (NC1) triggers necrosis by sodium overload (NECSO), the underlying mechanism remains to be elucidated. Here, we demonstrate that Na⁺ influx promotes necrosis by suppressing mitochondrial energy production. TRPM4-mediated Na⁺ entry elevates mitochondrial Na⁺ and reduces mitochondrial Ca²⁺ via NCLX, inhibiting oxidative phosphorylation and the Trichloroacetic acid (TCA) cycle, leading to severe energy depletion. This results in Na/K-ATPase inactivation, loss of ion gradients, cellular swelling and lysis. Our study reveals how sodium overload in NECSO disrupts mitochondrial metabolism to cause energy failure, potentially underlying diseases with elevated Na⁺.

Na⁺ is the most abundant cation in extracellular fluid. Normal concentrations of Na⁺ in extracellular fluid (ECF) range from 135 to 145 mmol/L, while the concentrations of Na⁺ inside cells (intracellular fluid) are -10–12 mmol/L¹. Maintaining this transmembrane concentration gradient is crucial for establishing the resting membrane potential and facilitating nutrient (such as glucose, amino acids, etc.) transport across cell membranes². The Na⁺ gradient is also pivotal in osmoregulation and water balance because Na⁺, accounting for 90% of ECF osmolality in combination with associated anions in mammalian cells³, drives water via osmosis to the direction of elevated Na⁺ concentration. Therefore, the maintenance of the Na⁺ gradient is vital for cellular homeostasis and the preservation of cell volume. In order to stabilize Na⁺ gradients, organisms have evolved complex mechanisms, including ion transport proteins (e.g., Na⁺/Ca²⁺ exchanger)⁴, ion channels (e.g., TRP channels)⁵, and ion pumps like Na/K-ATPase⁶. Central to this regulation, Na/K-ATPase is pivotal in maintaining the transmembrane gradients of Na⁺ and K⁺. By harnessing the energy from hydrolyzing one ATP molecule, the pump expels three Na⁺ from the cell and imports two K⁺ into the cell⁶. A significant portion of the cellular energy

expenditure is devoted to sustaining the normal operation of the Na/K-ATPase, particularly in neurons⁷, underscoring the importance of Na⁺ homeostasis in cellular function.

The collapse of the Na⁺ gradient and subsequent swelling of the cell seem to be a common feature in various types of necrosis. In the process of necroptosis, MLKL polymers form pores in the cellular membrane^{8,9}. During pyroptosis, the GSDM-NT fragment binds to and induces pore formation in the cellular membrane^{10,11}. In the case of ferroptosis, lipid peroxidation increases membrane tension, leading to the activation of Piezo¹². These distinct programmed cell death pathways ultimately result in a similar consequence: a substantial influx of Na⁺ and water into the cell. The prevailing understanding from current research suggests that Na⁺ influx occurs predominantly at the late stage of cell death, subsequent to plasma membrane damage, and its role in executing cell death is largely attributed to the disruption of osmotic balance. However, a key question that requires further elucidation centers on the potential of Na⁺ influx to operate not just as a consequence, but as an initiating regulator in the cell death cascade.

¹Department of Cardiology and Pediatric Translational Medicine Institute, Shanghai Children's Medical Center, Shanghai Jiao Tong University School of Medicine, Shanghai, China. ²Institute for Translational Medicine on Cell Fate and Disease, Shanghai Ninth People's Hospital, Key Laboratory of Cell Differentiation and Apoptosis of National Ministry of Education, Department of Pathophysiology, Shanghai Jiao Tong University School of Medicine, Shanghai, China. ³School of Pharmaceutical Sciences, Tsinghua University, Beijing, China. ⁴Tsinghua-Peking Joint Center for Life Sciences, Tsinghua University, Beijing, China. ✉ e-mail: fuwan@shsmu.edu.cn; zeping_hu@tsinghua.edu.cn; qingzhong@shsmu.edu.cn

The consequence of Na⁺ influx in the cytoplasm remains elusive. It has been shown that hypoxia can induce Na⁺ entry into mitochondria via the mitochondrial Na⁺/Ca²⁺ exchanger (NCLX). Once inside the mitochondria, Na⁺ interacts with phospholipids, thereby reducing the fluidity of the inner mitochondrial membrane and impeding the migration of free ubiquinone between Complex II and Complex III. This process inhibits oxidative phosphorylation (OXPHOS) function and fosters the production of reactive oxygen species (ROS)¹³. This research implies the potential of Na⁺ to influence mitochondrial energetics directly. However, the exact role of mitochondrial Na⁺ in promoting cell death requires further investigation. Under normal conditions, the concentration of Na⁺ inside mitochondria is lower than that in the cytosol. In respiring mitochondria, the concentration of Na⁺ in the mitochondrial matrix can be as much as 8 times lower than that in the cytosol^{14,15}. NCLX, located on the inner mitochondrial membrane¹⁶, serves as a pivotal pathway for Na⁺ influx into the mitochondria¹³. In studies using isolated mitochondria, it has been demonstrated that an elevation in extra-mitochondrial Na⁺ concentration can activate the transport activity mediated by NCLX¹⁷. Nevertheless, the role of NCLX in mediating the effects of increased cytosolic Na⁺ on mitochondrial function and cell death is yet to be fully understood.

In our previous study, we identified a form of necrosis driven by Na⁺ overload, termed necrosis induced by sodium overload (NECSO)^{18,19}. Unlike conventional forms of necrosis, NECSO is triggered by the activation of the monovalent cation channel Transient Receptor Potential Melastatin 4 (TRPM4), leading to substantial Na⁺ influx¹⁹. What distinguishes NECSO is its independence from well-characterized cell death pathways, such as apoptosis, necroptosis, ferroptosis, and pyroptosis, with Na⁺ acting as the key effector of cell death. Notably, classic features of apoptosis, such as chromatin fragmentation and caspase activation, are not observed in NECSO¹⁹. Moreover, inhibitors of apoptosis, necroptosis, and ferroptosis cannot block NECSO. Similarly, genetic depletion of key mediators like BAX, BAK, MLKL, ACSL4, and GSDMD does not prevent NECSO either¹⁸. However, TRPM4 knockout completely abolished Na⁺ influx and the subsequent necrotic process¹⁹.

In this study, we aim to uncover how Na⁺ influx, specifically through TRPM4 activation, influences mitochondrial functionality and contributes to necrosis. Utilizing the chemical agonist Necrocid 1 (NC1) to selectively activate TRPM4 provides a potent tool to further investigate the mechanisms underlying Na⁺ influx-induced necrosis. We propose that, by disrupting mitochondrial energy homeostasis and ionic balance, Na⁺ functions as an active initiator of necrosis, rather than merely a late-stage player in osmotic disruption. This study not only expands our understanding of necrosis but also potentially reveals the regulatory role of Na⁺ in pathological injuries characterized by elevated sodium levels.

Results

Sodium overload triggers energy depletion and mitochondrial ionic imbalance prior to cell rupture in NECSO

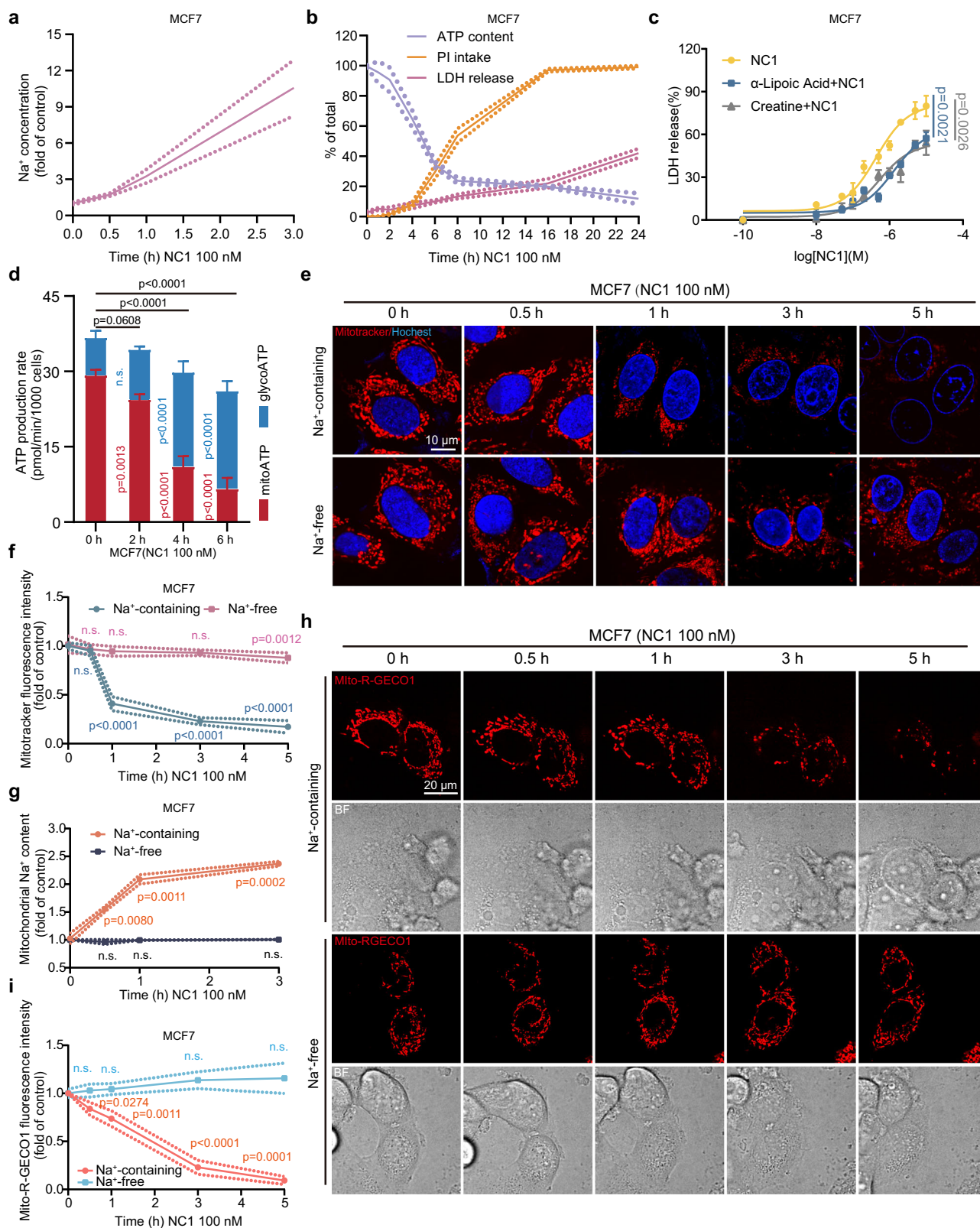
We initially utilized inductively coupled plasma-mass spectrometry (ICP-MS) to measure the intracellular concentration of Na⁺ in MCF7 cells that were treated with 100 nM NC1 at different time intervals, enabling us to investigate the dynamic changes in Na⁺ levels attributed to the NC1 treatment. We observed that a 30-min treatment with NC1 is sufficient to elevate intracellular sodium levels, which escalated over time with extended NC1 exposure (Fig. 1a). This indicates that sodium influx is initiated early upon NC1 treatment and persists over time.

To further confirm that sodium influx is an early event in NECSO, we subsequently monitored the time course of cell death in NC1-treated MCF7 cells. Concurrently, we assessed cellular ATP levels by CellTiterGlo and membrane integrity through propidium iodide (PI) staining positivity and lactate dehydrogenase (LDH) release.

Interestingly, we found a marked decline in intracellular ATP levels prior to an increase in membrane permeability, implying a potential causal relationship (Fig. 1b). Specifically, following NC1 treatment for 2 h, a decline of -10% in ATP levels was observed. After 4 h of NC1 treatment, ATP levels dropped to 60%, while <10% of the cells were PI positive. After 18 h, the percentage of cells staining positive for PI approached 100%. LDH release lagged behind PI positivity (Fig. 1b). The delayed release of LDH, given its large molecular size (135–145 kDa), may be attributed to the requirement for more extensive membrane damage to form larger pores than those permeable to PI. Similarly, in MB468 cells, our findings showed that the decline in intracellular ATP levels, post NC1 treatment, initiated earlier and proceeded at a faster rate compared to the increase in membrane permeability (Supplementary Fig. 1a). As a control, when MB468 cells were treated with 1 μM RSL3 to induce ferroptosis, we observed no discernible difference in the timing or rate of decline in intracellular ATP levels compared to the increase of membrane permeability (Supplementary Fig. 1b). Furthermore, a distinguishing feature was noted: in NECSO, LDH release was delayed compared to PI positivity, while in ferroptosis, LDH release closely followed PI positivity (Supplementary Fig. 1a, b), suggesting that the membrane damage in NECSO was more gentle and gradual compared with what observed in ferroptosis. In summary, our findings establish that sodium influx occurs during the earliest period post-NC1 treatment and suggest that energy depletion may contribute to subsequent membrane rupture. We further investigated the role of compounds that promote ATP generation, such as creatine and lipoic acid, in NECSO. Creatine is phosphorylated by creatine kinase to produce phosphocreatine (PCr), a high-energy compound. Upon degradation, PCr releases energy that is used to regenerate ATP from ADP and inorganic phosphate (Pi), thereby rapidly replenishing cellular ATP reserves and maintaining energy homeostasis²⁰. α-Lipoic acid, an essential cofactor for mitochondrial metabolism, enhances the activity of mitochondrial enzymes involved in energy metabolism and ATP production²¹. Notably, both creatine and α-lipoic acid were found to inhibit LDH release in NECSO (Fig. 1c).

Next, it is imperative to ascertain whether the depletion of cellular energy is a direct consequence of sodium influx. To block sodium influx, we used a Na⁺-free isotonic extracellular buffer solution (EBS) without serum or amino acids, in which Na⁺ was replaced by equimolar non-permeable NMDG⁺ to preserve iso-osmolality. A standard Na⁺-containing EBS served as control. The treatment was limited to 8 h to elicit NC1's effect while minimizing starvation-induced cell death. The ICP-MS analysis confirmed that sodium influx was completely abolished in NC1-treated MCF7 cells cultured in Na⁺-free medium (Supplementary Fig. 1c). Treatment with 100 nM NC1 in MCF7 cells cultured in Na⁺-free medium resulted in constant intracellular ATP levels, implying the significance of sodium influx in mediating ATP fluctuations. Accordingly, there was no detection of PI staining or LDH efflux, suggesting that the cellular membrane remained intact. In contrast, MCF7 cells treated with NC1 in Na⁺-containing EBS showed a decrease in ATP levels at an early stage, followed by positive PI staining and LDH release (Supplementary Fig. 1e, f). Similarly, NC1 treatment of MB468 cells also induced early sodium influx, followed by a sodium-dependent decline in ATP levels and subsequent membrane rupture (Supplementary Fig. 1g–i).

Further, we used Seahorse XF technology to quantify cellular ATP production rate in MCF7 cells treated with NC1. The findings revealed that in the control group, a majority of the ATP in MCF7 cells is derived from mitochondrial oxidative phosphorylation (mitoATP). Notably, following treatment with NC1, the mitoATP production rate decreased while the ATP production rate by glycolysis (glycoATP) increased compensatorily. However, the total ATP production rate declined (Fig. 1d). The data confirm that NC1 induces energy depletion, pointing to mitochondria as the main reason for energy production shortfall. To further investigate whether sodium influx contributes to the decrease



in ATP production rate, we measured the ATP synthesis rate following NC1 treatment in both Na⁺-containing and Na⁺-free EBS. In Na⁺-containing EBS, NC1 treatment led to a significant reduction in the overall ATP production rate, primarily due to decreased mitoATP generation, accompanied by a compensatory increase in glycoATP production (Supplementary Fig. 2a). In contrast, NC1 treatment in Na⁺-free EBS had no notable effect on ATP synthesis rate (Supplementary Fig. 2b).

Thus, we further investigated whether NC1 could cause damage to the mitochondria. We employed transmission electron microscopy (TEM) to examine the ultrastructural alterations of mitochondria in MCF7 cells following treatment with NC1. We observed that, as early as 30 min post-NC1 treatment, mitochondrial swelling commenced. After one hour of NC1 exposure, mitochondrial swelling became more pronounced. At three hours, severe cristae damage occurred, with

Fig. 1 | NCI-induced energy depletion and mitochondrial ionic imbalance are dependent on sodium influx. **a** $[Na^+]$ determined by ICP-MS for MCF7 cells treated with 100 nM NCI over time. **b** Time course of ATP levels, PI uptake, and LDH release in NCI-treated MCF7 cells in DMEM. **c** Effect of α -lipoic acid (2 mM) or creatine (0.2 mM) pre-treatment on NCI-induced LDH release (24 h). Data are mean \pm SD of triplicate samples from one representative of three independent experiments; statistical analysis: two-way ANOVA. **d** Glycolytic (glycoATP) and mitochondrial (mitoATP) ATP production rates in MCF7 cells treated with 50 nM NCI were measured using Seahorse XF technology. ATP levels (mitoATP: red; glycoATP: blue; total ATP: black) were compared to the control using one-way ANOVA. Data are mean \pm SD, $n = 4$ replicates from one representative of three independent experiments. P values (NCI vs. control at 2, 4, 6 h, respectively): total ATP: 0.0608, <0.0001 , <0.0001 ; mitoATP: 0.0013, <0.0001 , <0.0001 ; glycoATP: NS, <0.0001 , <0.0001 . **e** Representative confocal images of MitoTracker-stained MCF7 cells

treated with 100 nM NCI in Na^+ -containing or Na^+ -free EBS at the indicated times. Representative images are from three independent biological replicates.

f Quantification of mitochondrial fluorescence from **(e)**. Each group was compared to its 0-h control using one-way ANOVA, $n = 6$. P values (NCI vs. control): Na^+ -containing: n.s., n.s., n.s., 0.0012; Na^+ -free: n.s., <0.0001 , <0.0001 (0.5, 1, 3, 5 h). **g** Mitochondrial Na^+ levels in MCF7 cells after treatment with 100 nM NCI in Na^+ -containing or Na^+ -free EBS for 0.5, 1, or 3 h. Groups were compared to their respective 0-h controls (one-way ANOVA, $n = 3$). **h** Representative time-lapse images of mitochondrial Ca^{2+} in MCF7 cells expressing mito-R-GECO1 treated with 100 nM NCI in Na^+ -containing or Na^+ -free EBS. **i** Quantification of mito-R-GECO1 fluorescence from **(h)**. Data are mean \pm SD, $n = 3$. Each group was compared to its 0-h control (one-way ANOVA). P values (NCI vs. control): Na^+ -containing: n.s., n.s., n.s.; Na^+ -free: n.s., 0.0274, 0.0001, <0.0001 , 0.0001 (0.5, 1, 3, 5 h). Source data are provided in the Source Data file.

inner membrane blebs and lowered matrix density. By five hours, cristae were largely disassembled, and the intermembrane space was notably expanded. These findings demonstrate that mitochondrial swelling progresses progressively with extended exposure to NCI (Supplementary Fig. 2c). However, when Na^+ was equimolarly substituted with $NMDG^+$, NCI treatment did not induce mitochondrial swelling; rather, shrinkage of the mitochondria was observed following 3 and 5 h of treatment with NCI (Supplementary Fig. 2c). This may attribute to the displacement of Na^+ by $NMDG^+$, which blocks NCI-induced Na^+ influx (Supplementary Fig. 1c) but does not block NCI-induced K^+ efflux (Supplementary Fig. 1d) as potassium homeostasis is the main regulator of the mitochondrial matrix volume²². Mitochondria possess various K^+ channels that permit K^+ to move along their electrochemical gradient²³, and the efflux of K^+ from mitochondria leads to shrinkage of the matrix. We also employed Mitotracker Red to label mitochondria, finding that under conditions with Na^+ present, NCI treatment led to a weakening in Mitotracker Red signal, indicative of mitochondrial damage. In contrast, in the absence of extracellular Na^+ , Mitotracker Red signal was maintained following NCI treatment (Fig. 1e, f).

Given the importance of mitochondrial ionic imbalance to mitochondrial swelling, we studied whether NCI disturbs mitochondrial ionic balance. Exposure of MCF7 cells to NCI in Na^+ -containing EBS resulted in elevated $[Na^+]_{mito}$ (Fig. 1g) and reduced $[Ca^{2+}]_{mito}$, as measured using both the genetically encoded sensor mito-RGECO1 (Fig. 1h, i) and the Rhod-2 AM probe (Supplementary Fig. 2d–f). However, the changes of $[Na^+]_{mito}$ and $[Ca^{2+}]_{mito}$ were prevented by Na^+ depletion (Fig. 1g–i, Supplementary Fig. 2d–f). Collectively, these data demonstrate that NCI induces energy depletion and mitochondrial ionic imbalance prior to cell rupture, which depends on sodium influx.

Mitochondrial respiration is inhibited in NECSO

To further assess mitochondrial function, we evaluated mitochondrial respiratory capacity by measuring the oxygen consumption rate (OCR). Seahorse profile revealed that maximal respiration of MCF7 cells significantly reduced after NCI exposure. As the duration of NCI treatment on cells increases, the extent of suppression of maximal respiration gradually intensifies. After NCI treatment of MCF7 cells for 5 hours, the basal respiration was also significantly inhibited (Fig. 2a–c). Consistently, in MB468 cells, OCR was also observed to decrease upon processing of NCI (Supplementary Fig. 3a–c). We next used tetramethyl rhodamine ethyl ester (TMRE) to test whether NCI led to changes in mitochondrial membrane potential (Ψ_m). The live cell images showed that NCI led to a progressive collapse of Ψ_m (Fig. 2d). The decrease of Ψ_m was also confirmed by FACS (Fig. 2e).

Recent studies have suggested that Na^+ can inhibit the activity of mitochondrial Complex II + III^{15,24,25}. Since NCI triggers sodium influx, we explored whether the Na^+ accumulation in the cytoplasm, induced by NCI, could attenuate the function of the mitochondrial Electron

Transport Chain (ETC). We initially assessed the activity of Complex II in MCF7 cells following treatment with NCI. The results showed that the activity of Complex II decreased after treatment with NCI (Fig. 2f). To further substantiate the direct impact of elevated cytoplasmic Na^+ on ETC and rule out potential confounding effects of intracellular compensatory mechanisms, we assessed the activity of isolated mitochondrial Complex II + III under escalating concentrations of $NaCl$ within a cell-free system. The result showed that high salt inhibited Complex II + III activity in intact mitochondria in a dose-dependent manner (Fig. 2g).

Mitochondrial oxidative phosphorylation (OXPHOS) and glycolysis in the cytosol are both major pathways for cellular energy production. To assess the contribution of mitochondrial metabolism as an energy source in NECSO, we substituted galactose for glucose in the culture medium. Galactose, which is processed more slowly via the Leloir pathway than glucose in glycolysis²⁶ and yields no net ATP in glycolysis²⁷, effectively dampens glycolysis and shifts metabolism towards greater mitochondrial reliance²⁸. The results indicated that cells with a greater dependence on mitochondrial oxidative phosphorylation are more sensitive to NCI than cells utilizing glycolysis (Fig. 2h), implying that the suppression of mitochondrial energy generation by NCI promotes NECSO.

TCA cycle is inhibited in NECSO

Mitochondria, in addition to playing a crucial role in energy production, have significant functions in cellular metabolism. To uncover metabolic features of NCI-treated cells, we employed liquid chromatography–mass spectrometry (LC–MS)-based targeted metabolomics to investigate intracellular metabolite alterations in MCF7 cells after NCI treatment. Notably, pathway analysis revealed that the TCA cycle was significantly altered by NCI exposure (Fig. 3a and Supplementary Data 1).

Further, we specifically analyzed changes in TCA cycle-related metabolites at various time points post NCI treatment. Metabolite profiling revealed that prolonged NCI exposure led to a time-dependent accumulation of key TCA cycle intermediates, including isocitrate, α -ketoglutarate, succinate, fumarate, and malate (Fig. 3b and Supplementary Data 1). Such a concurrent increase signifies a substantial obstruction in the TCA cycle's flow. Since mitochondrial Ca^{2+} is crucial for activating mitochondrial metabolism and three key TCA cycle enzymes—pyruvate dehydrogenase (PDH)²⁹, isocitrate dehydrogenase (IDH)³⁰, and α -ketoglutarate dehydrogenase (AKGDH)³¹, the suppression of the TCA cycle observed in NCI-treated cells is likely due to a decline in $[Ca^{2+}]_{mito}$ (Fig. 1h, Supplementary Fig. 2d). Supportively, inhibition of MCU, the main channel for mitochondrial calcium uptake, by either siRNAs or inhibitors (DS16570511, RuRed) further exacerbated NECSO (Supplementary Fig. 4a, b). Pyruvate is converted to acetyl-CoA in the mitochondrial matrix by the pyruvate dehydrogenase complex (PDHc), fueling the TCA cycle

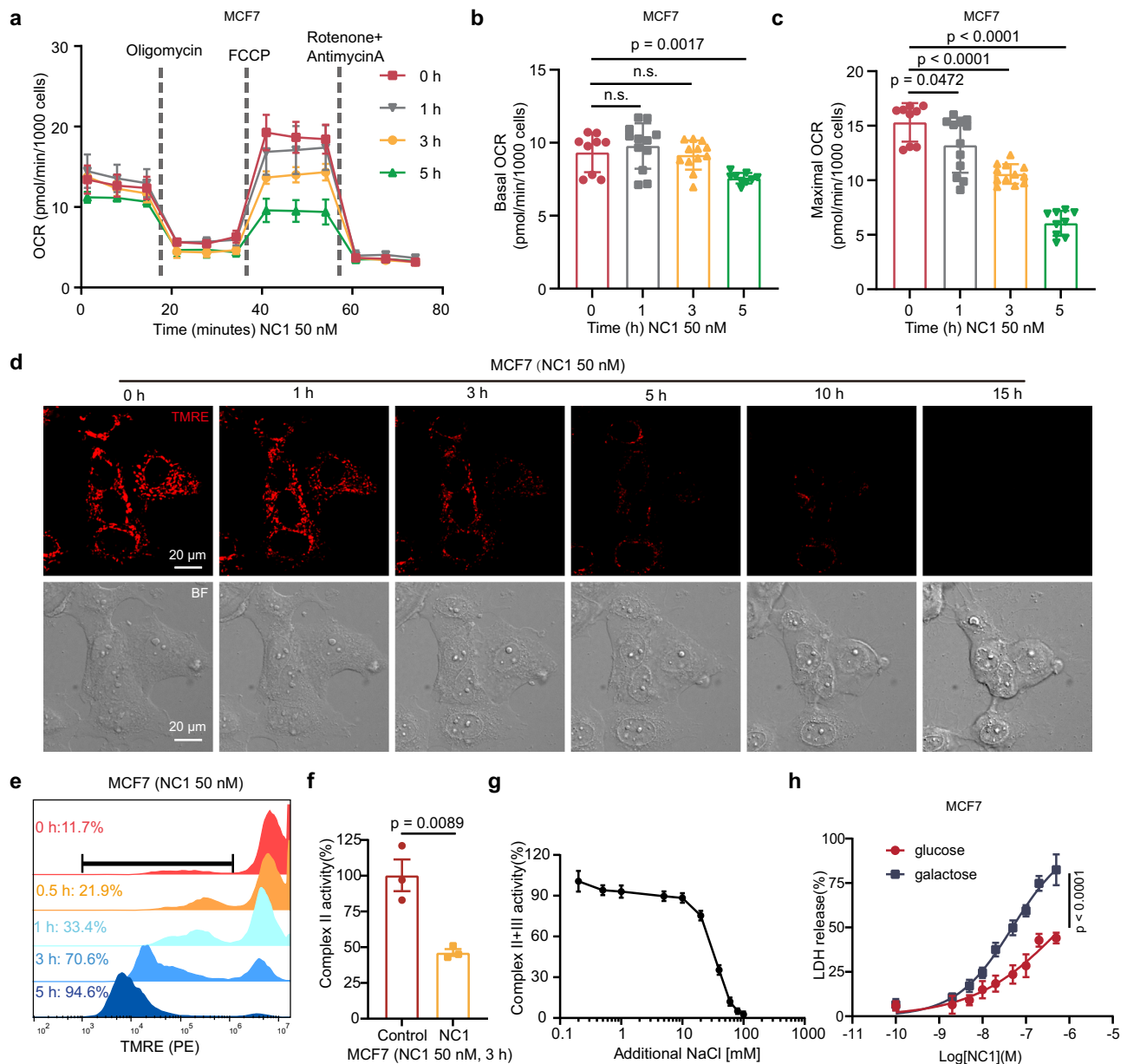


Fig. 2 | Mitochondrial respiration is inhibited in NECSO. **a** OCR of MCF7 cells treated with 50 nM NCI for indicated periods. Statistical analysis of basal OCR (**b**) and maximal OCR (**c**) in **a**, $n = 9$ (1, 5 h groups) and $n = 12$ (0, 3 h groups) from 3 independent experiments. Statistical analysis was conducted using a one-way ANOVA. Data are shown as mean \pm SD. P values (NCI vs. control, at 1, 3, 5 h): Basal OCR, n.s., n.s., 0.0017; Maximal OCR, 0.0472, <0.0001, <0.0001. **d** MCF7 cells were preloaded with TMRE dye and treated with 50 nM NCI. The mitochondrial membrane potential was detected via live-cell imaging using a confocal microscope. Representative images are from three independent biological replicates. **e** MCF7 cells preloaded with TMRE were treated with 50 nM NCI at the indicated times, and

mitochondrial membrane potential was assessed by FACS. **f** Complex II activity of MCF7 cells treated with 50 nM NCI for 3 h ($n = 3$ independent experiments, data are shown as mean \pm SD). Statistical analysis was conducted using an unpaired two-tailed t -test. **g** Complex II + III activity of bovine heart mitochondria under increasing concentrations of additional NaCl (0.0625–64 mM) ($n = 3$ independent experiments, data are shown as mean \pm SD). **h** LDH release of MCF7 cells cultured in glucose-free DMEM added with 40 mM glucose or galactose in the presence of NCI ($n = 3$ wells from 1 representative of 3 independent experiments). Statistical analysis was conducted using a two-way ANOVA, $p < 0.0001$. Data are shown as mean \pm SD. Source data are provided as a Source Data file.

(Fig. 3c). The PDHc comprises three domains: pyruvate dehydrogenase (PDH, E1), dihydrolipoyl transacetylase (E2), and dihydrolipoyl dehydrogenase (E3). Thiamine diphosphate (TPP) is an essential cofactor for pyruvate dehydrogenase³². The accumulation of pyruvate and TPP indicates a disruption in pyruvate metabolism. Moreover, phosphorylation of the E1 alpha 1 subunit (PDHA1) at Ser293, which inactivates PDHc³³, increased progressively with NCI treatment duration (Supplementary Fig. 4c). This provides further evidence that PDHc activity is attenuated during NECSO.

In Fig. 3b, succinate exhibited the most pronounced accumulation, with a noticeable increase in its levels even at an early stage (30 min) after NCI treatment. Considering that the accumulation of succinate might be due to suppression of the conversion of succinate to fumarate catalyzed by succinate dehydrogenase (SDH, also known as Mitochondrial Complex II)³⁴, we next evaluated the succinate/fumarate ratio. SDH serves as the hub connecting the TCA cycle and oxidative phosphorylation, which facilitates the transfer of electrons from succinate to

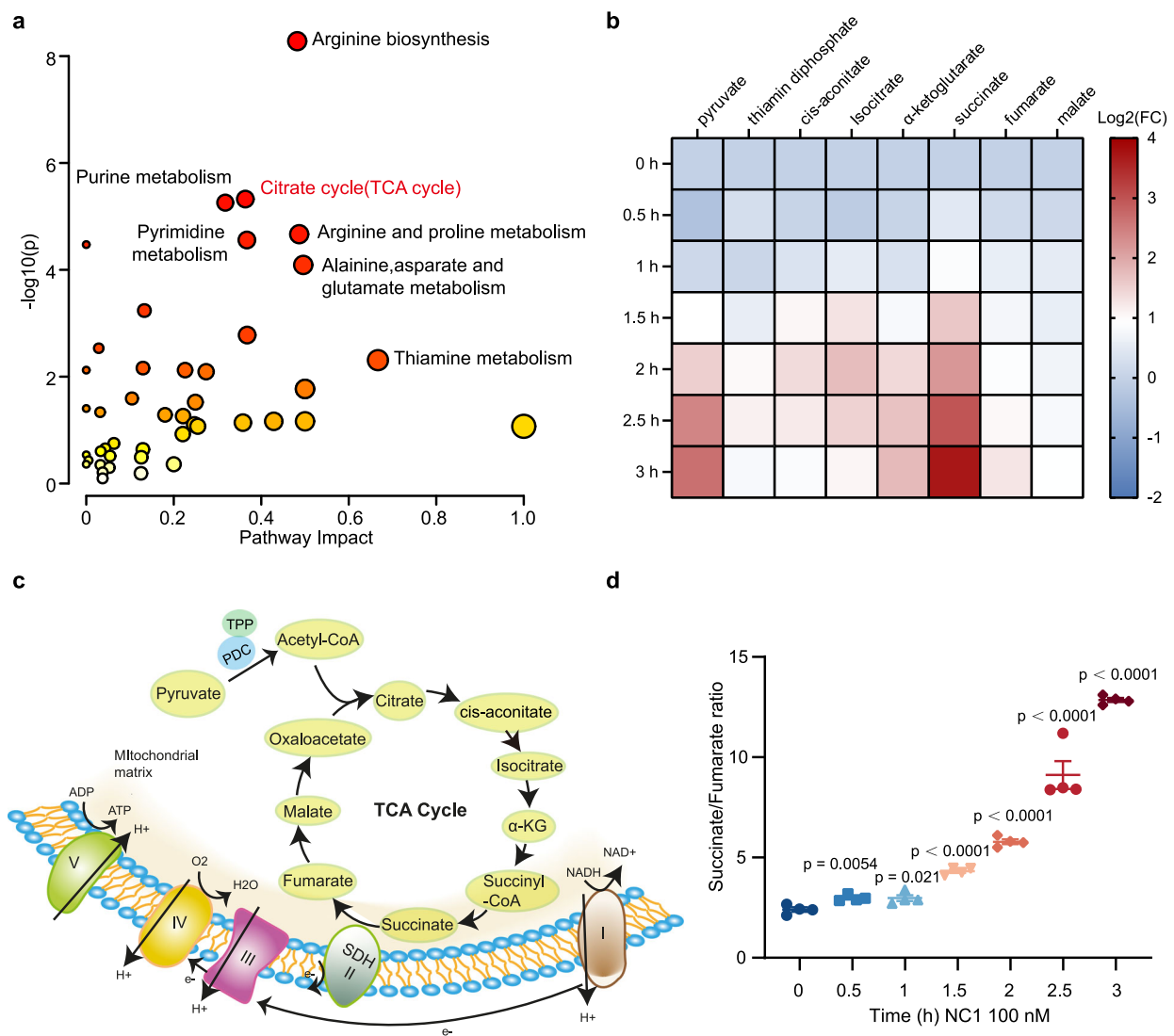


Fig. 3 | TCA cycle is inhibited in NECSO. a KEGG metabolic pathways enriched by significantly differential metabolites between MCF7 cells treated with 100 nM NC1 for 3 h and control cells. One-sided Fisher's exact test followed by BH multiple comparison tests was used, and only pathways with FDR < 0.05 were presented. **b** Heatmap displaying the differential metabolites in the TCA cycle of MCF7 cells treated with 100 nM NC1 for 0.5, 1, 1.5, 2, 2.5, or 3 h. Each group had four replicates, normalized to the 0-h control values. **c** A schematic diagram illustrating the TCA cycle and oxidative phosphorylation, connected by SDH (Complex II). **d** MCF7 cells,

which were treated with 100 nM NC1 at different times as indicated, the ratio of the metabolites succinate to fumarate was calculated at each time point ($n = 4$ independent samples). The ratios at different times were compared with the ratio of 0-h control group, respectively. A one-way ANOVA was performed; the data are shown as mean \pm SD. *P* values (NC1 vs. control, at 0.5, 1, 1.5, 2, 2.5, 3 h): 0.0054, 0.0021, <0.0001, <0.0001, <0.0001, <0.0001. Source data are provided as a Source Data file.

ubiquinone while reducing succinate to fumarate (Fig. 3c). Results shown in Fig. 3d indicate that the succinate/fumarate ratio progressively increases with the extension of NC1 treatment time. This finding aligns with and supports the observation of reduced Complex II activity presented in Fig. 2f. Conclusively, the metabolic profiling provides compelling evidence for mitochondrial dysfunction in NC1-treated cells.

Sodium overload-induced mitochondrial dysfunction depends on mitochondrial NCLX

NCLX has been identified as a pivotal pathway mediating Na⁺ influx into mitochondria by exchanging mitochondrial Ca²⁺ to cytoplasm¹⁶. To ascertain whether NCLX mediates NC1-induced mitochondrial damage, we employed a specific inhibitor of NCLX (CGP37157, CGP)³⁵ in subsequent experiments. Notably, the NCLX

inhibition significantly mitigated the mitochondrial swelling induced by NC1, as shown by electron microscopy analysis (Fig. 4a). CGP markedly reversed not only the NC1-induced rise of [Na⁺]_{mito} (Fig. 4b), but also the reduction of [Ca²⁺]_{mito} (Fig. 4c), suggesting that NCLX plays a pivotal role in mediating the NC1-induced disturbance of mitochondrial ionic balance. Furthermore, CGP alleviated the decline of Ψ_m induced by NC1 (Fig. 4d). Seahorse profile also revealed that the inhibition of NCLX significantly rescued both maximal respiration and basal respiration reduction in cells treated with NC1 (Fig. 4e–g). In addition, CGP ameliorated the decrease in Complex II+III activity caused by high salt (Fig. 4h). Consistently, CGP mitigated the accumulation of TCA cycle metabolites (Supplementary Fig. 5a and Supplementary Data 2) and reduced the elevated succinate/fumarate ratio (Supplementary Fig. 5b) induced by NC1. In line with these

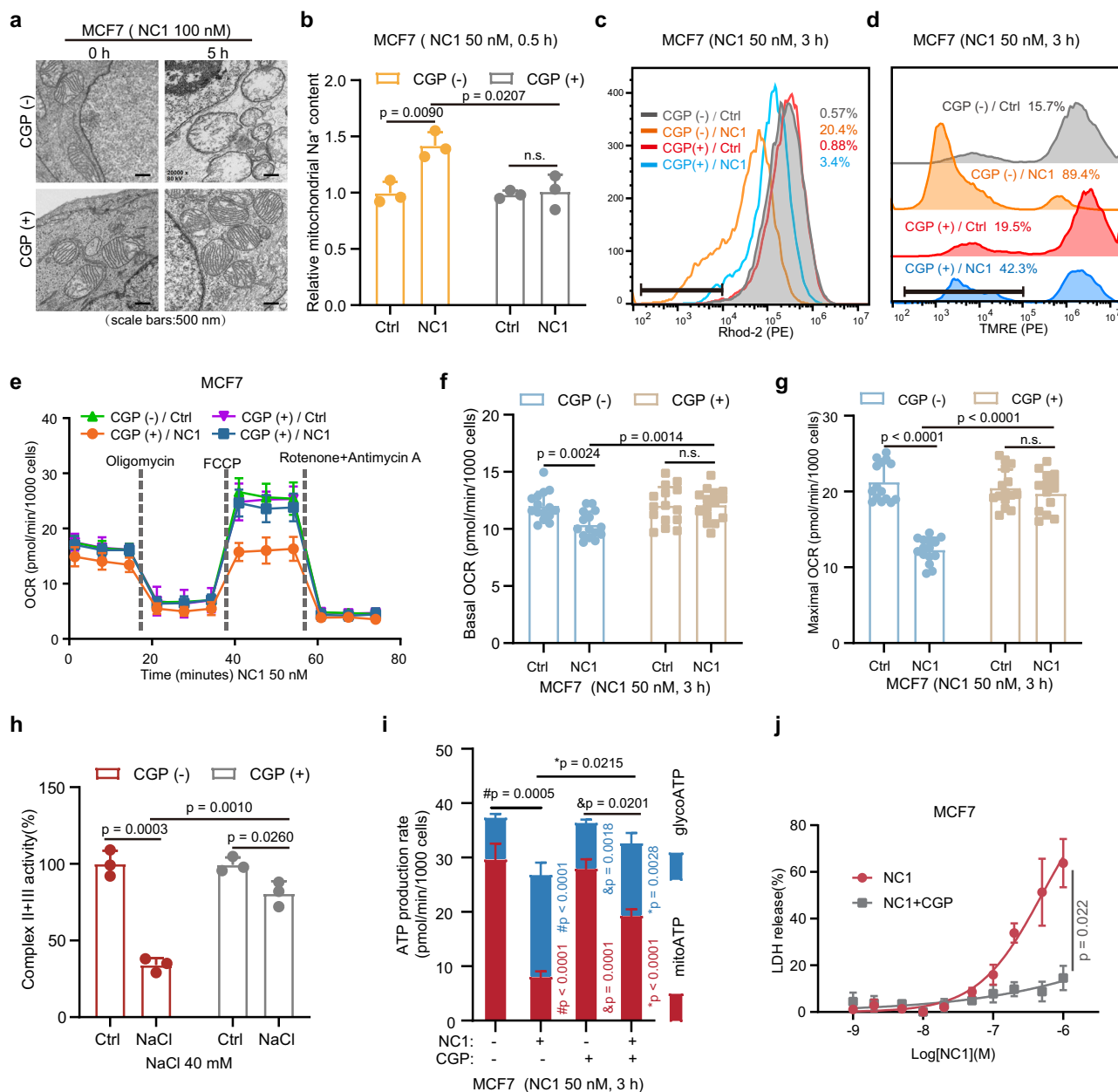


Fig. 4 | Inhibition of NCLX reverses NC1-induced mitochondrial dysfunction.

a Representative transmission electron microscopy images of MCF7 cells treated with 100 nM NC1 for 5 h with or without 20 μ M CGP37157 (CGP) pretreatment. Representative of three independent experiments. **b** Mitochondrial Na⁺ levels in MCF7 cells after 0.5 h treatment with 50 nM NC1 with or without CGP pretreatment ($n = 3$ independent experiments). **c** Rhod-2 AM-loaded MCF7 cells were treated with 50 nM NC1 for 3 h with or without CGP pretreatment. Mitochondrial Ca²⁺ was measured by FACS. **d** TMRE-loaded MCF7 cells were treated as in (c). Mitochondrial membrane potential was assessed by FACS. **e** OCR of MCF7 cells treated with 50 nM NC1 for 3 h with or without CGP pretreatment. Statistical analysis of basal (**f**) and maximal (**g**) OCR ($n = 15$ from 3 independent experiments). *P* values (NC1 vs. Ctrl, no CGP): 0.0024 (Basal), <0.0001 (Maximal); *P* values (NC1 vs. Ctrl, with CGP): n.s. (Basal), n.s. (Maximal); *P* values (+CGP vs. -CGP, NC1-treated): 0.0014 (Basal),

<0.0001 (Maximal). **h** Complex II + III activity in bovine heart mitochondria with additional 40 mM NaCl in the presence or absence of 20 μ M CGP ($n = 3$ independent experiments). **i** ATP production rates (mitoATP, glycoATP, total ATP) in MCF7 cells after 3 h NC1 treatment \pm CGP ($n = 4$ replicates from one representative of three independent experiments). Data are shown as mean \pm SD. *P* values: # (NC1 vs. Ctrl, no CGP): mitoATP <0.0001, glycoATP <0.0001, total ATP 0.0005; & (NC1 vs. Ctrl, +CGP): mitoATP 0.0001, glycoATP 0.0018, total ATP 0.0201; * (+CGP vs. -CGP, NC1-treated): mitoATP <0.0001, glycoATP 0.0028, total ATP 0.0215. Colors: red (mitoATP), blue (glycoATP), black (total ATP). **j** LDH release in MCF7 cells after 18 h NC1 treatment \pm CGP. A two-way ANOVA was performed, $n = 3$ wells from 1 representative of 3 independent experiments. Statistical analysis in **b**, **f**–**i** was conducted using an unpaired, two-tailed test. Data are all shown as mean \pm SD. Source data are provided as a Source Data file.

data, CGP augmented both the mitoATP synthesis rate and the overall ATP production rate in cells that were subjected to NC1 treatment (Fig. 4i). Obviously, CGP inhibited NC1-induced cell death (Fig. 4j). In summary, these results indicate that NC1-induced sodium influx exacerbates mitochondrial damage and facilitates cell death through NCLX.

Cellular energy depletion exacerbates monovalent cation gradients collapse by inhibiting the Na/K-ATPase in NCSO

One of the primary usages of cellular energy is to sustain the normal function of the Na/K-ATPase. The Na/K-ATPase maintains cellular osmotic pressure and homeostasis by pumping 3 Na⁺ out of the cells in exchange for 2K⁺, utilizing the energy derived from the hydrolysis

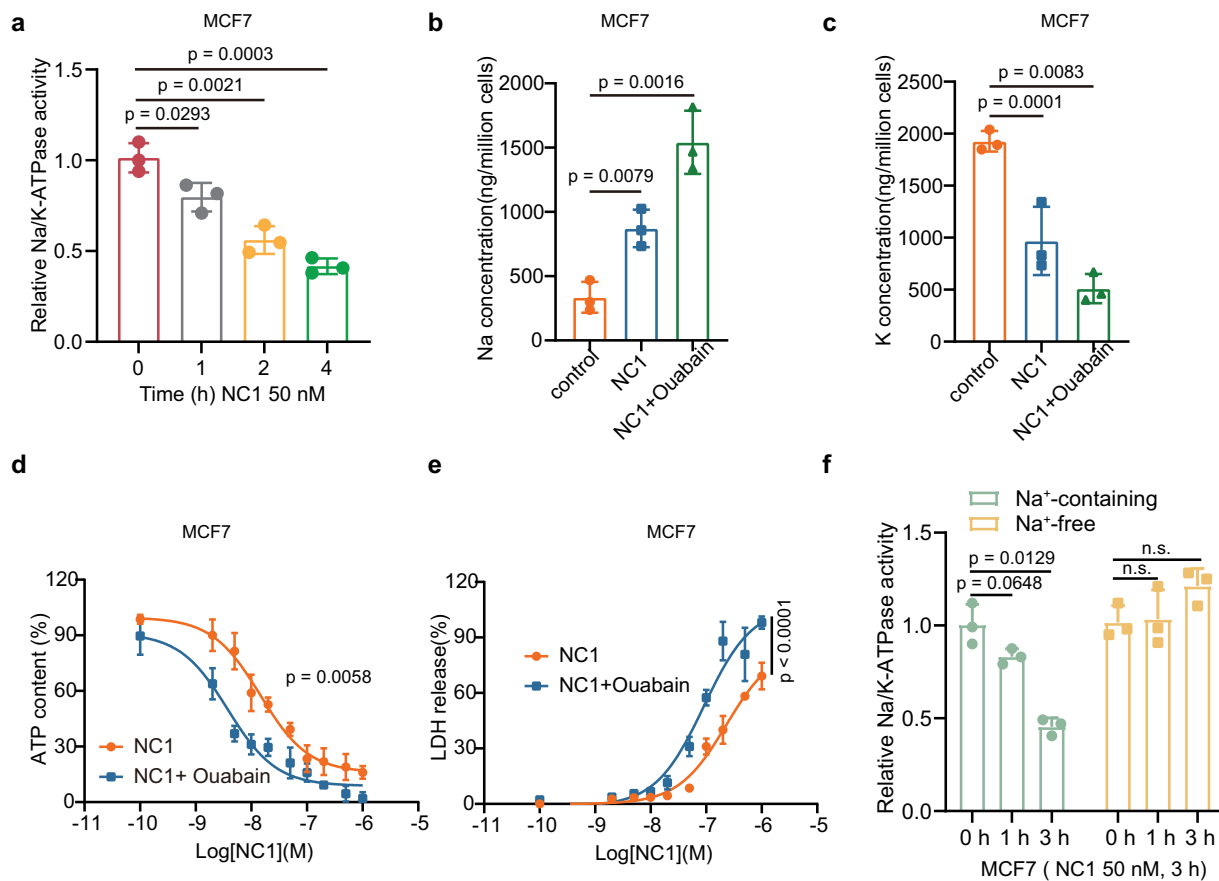


Fig. 5 | Energy depletion collapses monovalent cation gradients via the inhibition of the Na/K-ATPase. **a** Na/K-ATPase activity in MCF7 cells treated with 50 nM NC1 over time under normal DMEM ($n = 3$ independent experiments). **b** $[Na^+]$ determined by ICP-MS for MCF7 cells under normal DMEM culture condition treated with 50 nM NC1 for 3 h with or without 1 μ M ouabain pretreatment ($n = 3$ independent samples). **c** $[K^+]$ determined by ICP-MS for MCF7 cells under normal DMEM culture condition treated with 50 nM NC1 for 3 h with or without 1 μ M ouabain pretreatment ($n = 3$ independent samples). **d** ATP levels in MCF7 cells after

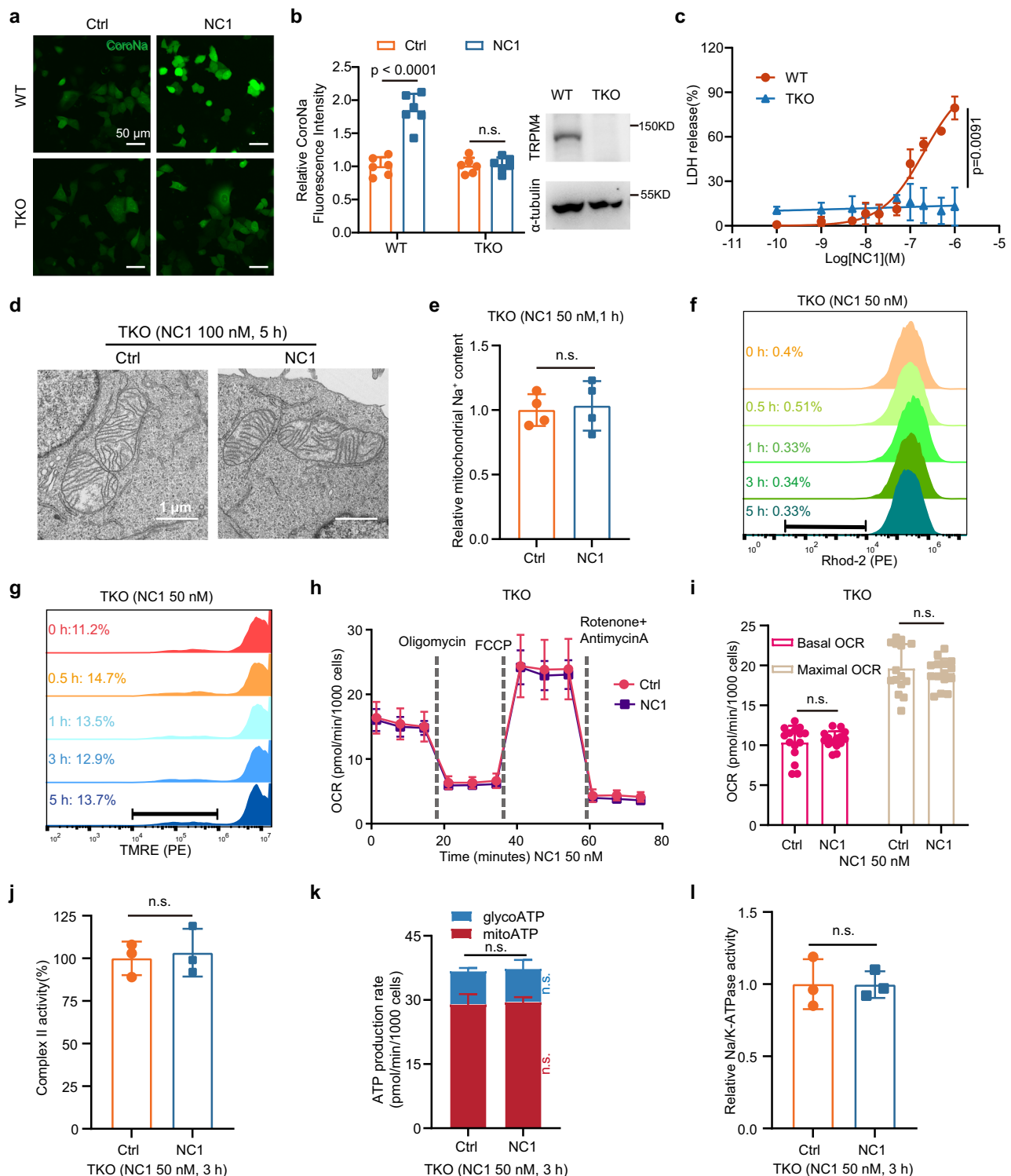
20-h NC1 treatment with or without 10 nM ouabain ($n = 3$ wells from 1 representative of 4 independent experiments). **e** LDH release from MCF7 cells after 20-h NC1 treatment with or without 10 nM ouabain ($n = 3$ wells from 1 representative of 4 independent experiments). Statistical significance: $p < 0.0001$. **f** Na/K-ATPase activity in MCF7 cells treated with 50 nM NC1 in Na^+ -containing or Na^+ -free extracellular buffer solution (EBS) over time ($n = 3$ independent experiments). Statistical analysis: one-way ANOVA (**a–c**, **f**); two-way ANOVA (**d** and **e**). Data are shown as mean \pm SD. Source data are provided as a Source Data file.

of a single ATP. Insufficient cellular energy supply can impair the activity of the Na/K-ATPase³⁶. We therefore investigated whether Na/K-ATPase activity was inhibited in NECSO. We quantified the portion of ATPase activity that is sensitive to ouabain (a well-known Na/K-ATPase inhibitor)³⁷ in a membrane-rich sample of cells, by employing malachite green to detect the phosphate liberated from ATP. As illustrated in Fig. 5a, the activity of Na/K-ATPase in MCF7 cells was inhibited after 1 hour of NC1 treatment, and further suppressed as NC1 exposure extended. Ouabain amplifies the NC1-induced ionic imbalance, characterized by an accumulation of Na^+ (Fig. 5b) and a reduction in K^+ (Fig. 5c). Furthermore, even a very low concentration of ouabain (10 nM) can exacerbate NC1-induced cell death (Fig. 5d, e). These results suggest that Na/K-ATPase inhibition plays a crucial role in the collapse of ion gradients and cell death induced by NC1. To determine whether the suppression of Na/K-ATPase activity is caused by NC1-induced sodium influx, we assessed Na/K-ATPase activity in cells treated with NC1 under Na^+ -free conditions, with Na^+ -containing EBS serving as the control. Our findings revealed that in the absence of extracellular sodium, NC1 did not lead to inhibition of Na/K-ATPase activity (Fig. 5f), thereby implicating sodium influx as a prerequisite for this effect. We further confirmed in MB468 cells that NC1 inhibited Na/K-ATPase activity in a sodium influx-dependent

manner (Fig. S6a, b), while ouabain promoted NECSO (Supplementary Fig. 6c, d).

TRPM4 is required for mitochondrial dysfunction and energy depletion in NECSO

Consistent with our previous work¹⁹, we have demonstrated that TRPM4 mediates the sodium influx (Fig. 6a) and necrosis induced by NC1 (Fig. 6b and c). In order to further confirm that NC1-induced mitochondrial damage is a consequence of elevated cytosolic sodium levels rather than direct NC1 action on mitochondria, we investigated whether NC1 retains its capacity to induce mitochondrial injury in TRPM4-knockout cells. Transmission electron microscopy observations of NC1-treated TRPM4-knockout cells revealed no significant differences in mitochondrial morphology compared to control cells (Fig. 6d). Furthermore, no discernible changes were observed in $[Na^+]_{mito}$ and $[Ca^{2+}]_{mito}$ following the administration of NC1 to TRPM4-knockout cells (Fig. 6e, f). Additionally, TRPM4-knockout completely abolished NC1-induced decrease of Ψ_m (Fig. 6g), oxygen consumption rate (Fig. 6h, i) and Complex II activity (Fig. 6j). Importantly, the administration of NC1 to TRPM4-knockout cells had no impact on either the ATP production rate (Fig. 6k) or the activity of the Na/K-ATPase (Fig. 6l). Consequently, the detailed mechanism illuminated by



our investigation suggests that NC1-induced sodium influx, mediated through TRPM4, initiates a series of events wherein NCLX facilitates the influx of Na⁺ into mitochondria while promoting the efflux of Ca²⁺ from the matrix. This imbalance in mitochondrial ionic homeostasis dampens mitochondrial energy production, which directly contributes to the inhibition of Na/K-ATPase activity.

Osmoprotectants and AQP4 inhibition suppress NECSO

Next, we want to clarify how, following the collapse of the ion gradients due to energy deficiency, NECSO is ultimately executed. The collapse

of the ion gradients elevates osmotic pressure, resulting in water influx, cell swelling, and the development of nanometer-scale membrane defects. Osmoprotectants with diameters larger than the membrane defects remain in the extracellular medium, where they counterbalance the increased intracellular osmolarity, thereby preventing water influx, swelling, and lysis (Fig. 7a). In contrast, osmoprotectants with smaller diameters do not exhibit this protective effect. Thus, we employed a series of osmoprotectants with different hydrated diameters, including sucrose (-0.9 nm), PEG 2K (-2.6 nm), PEG 4K (-3.2 nm), and PEG 8K (-4 nm)^{38,39}. The inhibition of LDH release

Fig. 6 | TRPM4 is required for mitochondrial dysfunction induced by NCl. **a** MCF7 WT cells and TRPM4 knockout (TKO) cells were loaded with Na⁺ indicator CoroNa Green and treated with 50 nM NCl for 2 h. Representative confocal images of three independent experiments are shown. **b** Quantification of mean fluorescence intensity from **(a)** ($n = 6$ independent images). P values (NCl vs. Ctrl): WT, $p < 0.0001$; TKO, not significant (n.s.). Right panel: TRPM4 protein expression in WT and TKO cells. **c** LDH release in WT and TKO cells after 24-h NCl treatment ($n = 3$ wells, one representative of two independent experiments). Statistical analysis by two-way ANOVA. **d** Representative transmission electron microscopy images of TKO cells treated with 100 nM NCl for 5 h (representative of three independent experiments). **e** Mitochondrial Na⁺ levels in TKO cells after 1-h NCl treatment (50 nM) ($n = 3$ independent experiments). **f** MCF7 TKO cells preloaded with Rhod-2

AM were treated with 50 nM NCl for the indicated times and analyzed by FACS to measure mitochondrial Ca²⁺. **g** TKO cells preloaded with TMRE were treated with 50 nM NCl for the indicated times and analyzed by FACS for mitochondrial membrane potential. **h** OCR of TKO cells after 3-h NCl treatment (50 nM). **i** Statistical analysis of basal and maximal OCR in **h** ($n = 15$ from 3 independent experiments). **j** ATP production rate in TKO cells after 3-h NCl treatment ($n = 4$ replicates, one representative of three independent experiments). **k** ETC Complex II activity in TKO cells after 3-h NCl treatment ($n = 3$ independent experiments). **l** Na/K-ATPase activity in TKO cells after 3-h NCl treatment ($n = 3$ independent experiments). Statistical analysis in **b**, **e**, **i**, **j**, and **l** was performed using an unpaired, two-tailed test. Data are shown as mean \pm SD. Source data are provided as a Source Data file.

by osmoprotectants was size-dependent, with PEG8K almost completely inhibiting NCl-induced LDH release (Fig. 7b). Moreover, PEG8K almost entirely inhibits NCl-induced cell swelling and PI uptake (Fig. 7c). This suggests that in NECSO, osmotic cell swelling leads to the formation of size-varying membrane defects, ultimately resulting in cell lysis. Intriguingly, aquaporins (AQPs) mediate water flow, among which AQP4 has been reported to form heterodimers with TRPM4⁴⁰. We therefore tested the effect of the AQP4 inhibitor AER-271 and AQP4 siRNAs in NECSO. The results showed that both pharmacological and genetic inhibition of AQP4 significantly reduced NCl-induced LDH release (Fig. 7d and e), suggesting that AQP4 plays a role in mediating water influx during NECSO.

In summary, our study reveals that NCl activates TRPM4, increasing sodium influx and intracellular sodium levels. This stimulates NCLX-mediated Na⁺ import and Ca²⁺ export from mitochondria, disrupting mitochondrial ionic balance and impairing energy generation via the TCA cycle and oxidative phosphorylation. Reduced ATP synthesis impairs Na/K-ATPase function, collapsing ion gradients. Ultimately, osmotic imbalance leads to cell swelling and membrane rupture, and AQP4 mediates the influx of water (Fig. 7f).

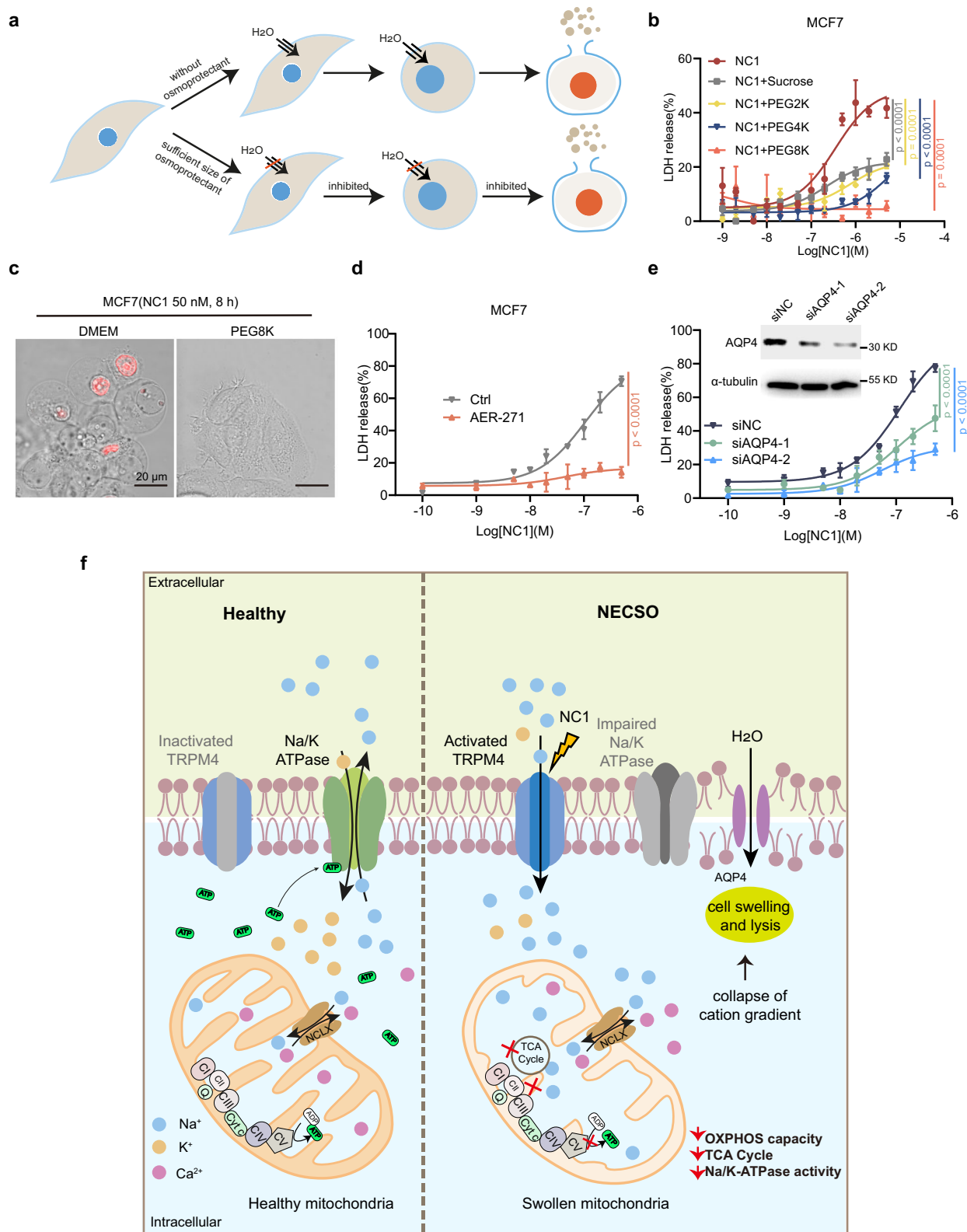
Discussion

Conventionally, the perception of the role Na⁺ plays in cell death has been largely confined to its effects on osmotic equilibrium. In this investigation, we present evidence that Na⁺ influx can orchestrate cell death by inhibiting mitochondrial energy production. Mechanistically, our study reveals that NCl-induced Na⁺ influx, reliant on TRPM4, activates NCLX-mediated transport, leading to an increase in [Na⁺]_{mito} and a decrease in [Ca²⁺]_{mito}. This perturbation impedes the TCA cycle, mitochondrial oxidative phosphorylation, and overall energy generation. Therefore, the activity of the Na/K-ATPase is compromised, ultimately triggering the collapse of intracellular cation gradients, promoting osmotically cellular swelling and membrane rupture.

Given that NCl loses its capacity to inflict mitochondrial damage in TRPM4 knock-out cells, coupled with the observation that sodium influx becomes evident in the early stages of NCl treatment in WT cells, we ruled out the possibility that NCl directly targets mitochondria to exert its effects. Instead, this evidence solidified our conviction that mitochondrial injury is a downstream consequence of TRPM4-mediated sodium influx induced by NCl. Sodium accumulating in the cytoplasm enters the mitochondria via NCLX, impairing mitochondrial respiration by affecting the activity of mitochondrial complexes II and III. This leads to a decline in mitochondrial oxidative phosphorylation capacity (OXPHOS) and ATP production. Consistent with our findings, Treg cells²⁵ and Mononuclear Phagocytes²⁴ under high salt circumstances similarly exhibited impaired mitochondrial respiration and energy production, which is attributed to the direct inhibitory effect of Na⁺ on mitochondrial complex II+III. These observations collectively suggest that the inhibitory effect of Na⁺ on OXPHOS might represent a universal mechanism operative across various cell types.

Ca²⁺ activates three key dehydrogenases of the TCA cycle^{29–31}, accelerating NADH production⁴¹. This enhances Electron Transport Chain (ETC) electron flow, boosting the proton motive force and ATP generation^{42,43}. Consequently, a decline in Ca²⁺_{mito} results in reduced mitochondrial energy generation. On the other hand, mitochondrial calcium overload can lead to the opening of mitochondrial permeability transition pore (MPTP)⁴⁴, inducing apoptosis or necrosis^{45,46}. Therefore, maintaining an optimal level of free calcium within the mitochondrial matrix is essential. Mitochondrial Ca²⁺ homeostasis relies on balanced Mitochondrial Calcium Uniporter (MCU) uptake⁴⁷ and NCLX efflux^{16,48}. Our results indicate a decrease in mitochondrial Ca²⁺ in NECSO, primarily mediated by NCLX. Furthermore, when we inhibited MCU function using either pharmacological inhibitors (DS16570511, RuRed) or siRNAs, thereby blocking mitochondrial calcium uptake, NECSO is exacerbated (Supplementary Fig. 4a, b). Collectively, these findings support our conclusion that NCl induces a decrease in mitochondrial calcium level, leading cells into a low-energy metabolic state. Thus, it is reasonable to conclude that elevated cytoplasmic Na⁺ impairs mitochondrial energy metabolism through dual mechanisms: inhibition of Complex II+III activity following mitochondrial entry, and disruption of the TCA cycle through enhanced mitochondrial calcium efflux.

Sodium overload is controlled by multiple mechanisms, including the opening of sodium channels⁴⁹ and diminished activity of the Na/K-ATPase⁵⁰. TRPM4-mediated sodium influx, induced by NCl, represents one pathway among these. A prior study indicates that the activation of NaV1.6 channels by Veratridine can result in mitochondrial Na⁺ uptake and Ca²⁺ efflux via the Na⁺/Ca²⁺ exchanger⁵¹. This observation supports that the mitochondrial Na⁺/Ca²⁺ exchanger may play a role under various scenarios involving increased cytoplasmic sodium. In addition, sodium overload can be observed in various pathological conditions, such as hypertonic external environment^{24,25}, infection⁵², hypertension⁵³, cardiac and cerebral ischemia^{54,55}, cardiac hypertrophy and failure⁵⁶. It is intriguing to speculate that under these conditions, Na⁺ may compromise mitochondrial metabolism through mechanisms akin to those discussed above, with NCLX serving as the pivotal target in this process. Pharmacological inhibition of NCLX can ameliorate cardiac metabolic dysregulation in heart failure⁵⁷, prevent sudden death associated with heart failure⁵⁸, and offer neuroprotection⁵⁹. However, complete genetic knockout of *Slc8b1* (encoding gene of NCLX) in adult mouse hearts is lethal⁴⁸. The challenge in targeting NCLX in vivo might be due to its critical role as the primary mediator of mitochondrial calcium efflux, and the complete inhibition of NCLX could lead to detrimental mitochondrial calcium overload^{48,60,61}. In contrast, CGP does not increase basal matrix calcium⁶². Therefore, it might be a more feasible strategy to utilize inhibitors to modulate NCLX function under specific pathologic conditions characterized by elevated cytoplasmic sodium. Although CGP exhibits specificity and selectivity towards NCLX in the context of cardiomyocyte³⁵, it has also been reported to affect the plasma membrane NCX3⁶³ and VGCC⁶⁴ in neuronal cells. Future research is necessary to overcome these issues.



Notably, extensive efforts have been made to optimize CGP's specificity and pharmacokinetics via new analog development^{59,65}, which hold promise for more effective therapeutic applications in the future.

The delayed LDH release relative to PI staining suggests that membrane rupture in NECSO is a regulated and progressive process. We propose that the initial sodium influx mediated by TRPM4 triggers energy depletion, which subsequently inhibits Na/K-ATPase activity—a

key mechanism driving the execution of NECSO. This inhibition leads to secondary cytoplasmic sodium accumulation and ultimately an ion imbalance. The resulting osmotic imbalance promotes water influx, leading to cell swelling and eventual membrane rupture. While it has been demonstrated that TRPM4 can form a hetero-multimeric complex with AQP4 to induce astrocytic swelling⁴⁰, the specific role of AQP4 in NECSO remains to be defined. Critically, we found that

Fig. 7 | Osmoprotectants and AQP4 inhibition block membrane rupture in NECSO. **a** Membrane defects allow water influx via the osmotic gradient created by intracellular macromolecules, leading to cell swelling and lysis. Osmoprotectants larger than the defects can prevent this effect. **b** Size-dependent inhibition of LDH release from NCI-treated MCF7 cells by osmoprotectants (20 mM in DMEM, 20-h treatment). All tested osmoprotectants significantly reduced LDH release ($p < 0.0001$ for Sucrose, PEG2K, PEG4K; $p = 0.0001$ for PEG8K). **c** Confocal images of MCF7 cells treated with 50 nM NCI for 8 h in DMEM with or without 20 mM PEG8K. Red fluorescence indicates PI-positive cells. Images are representative of three independent experiments. **d** LDH release of MCF7 cells treated with NCI for 24 h with or without 200 μ M AER-271 pretreatment. Statistical significance: $p < 0.0001$. **e** AQP4 siRNAs reduced NCI-induced LDH release in MCF7 cells after 24 h ($p < 0.0001$ for both siAQP4-1 and siAQP4-2). Western blot confirmed the knockdown efficiency of AQP4 siRNAs in MCF-7 cells. **f** Schematic overview of how

Na⁺ influx orchestrates NECSO. Under normal physiology, TRPM4 remains closed, permitting healthy mitochondria to sustain adequate energy production for the Na/K-ATPase. Upon NCI treatment, TRPM4 was open and mediated sodium influx. Overloaded intracellular Na⁺ enters the mitochondria through NCLX, leading to inhibition of OXPHOS and causing mitochondrial calcium decreases, which disrupts the TCA cycle. This impairs mitochondrial energy generation, leading to Na/K-ATPase suppression and ion gradient collapse. Subsequently, the elevated intracellular osmotic pressure drives water influx, resulting in cell swelling and progressive damage to the plasma membrane and eventual lysis. AQP4 may be involved in facilitating this substantial water entry. Data in **b**, **d**, and **e** were analyzed using a two-way ANOVA ($n = 3$ wells from 1 representative of 3 independent experiments) and shown as mean \pm SD. Source data are provided as a Source Data file.

functional inhibition of AQP4, either via specific siRNAs or the small-molecule inhibitor AER-271, significantly attenuated NECSO. Whether AQP4 forms a polymeric complex with TRPM4 to mediate NECSO remains to be determined. Furthermore, the application of osmoprotectants with increasing hydrodynamic diameters conferred progressively stronger protection against NECSO. Notably, PEG-8K (~4 nm hydrodynamic diameter) almost completely suppressed NECSO, indicating the presence of osmotic membrane injury during this process.

The involvement of mitochondria in programmed cell death has precedents. In apoptosis, mitochondria act as a “reservoir”, storing apoptosis-related proteins such as cytochrome *c*⁶⁶, OMI⁶⁷, and SMAC⁶⁸. During ferroptosis, the actions of mitochondria are associated with their metabolic activities that lead to the generation of reactive oxygen species (ROS)⁶⁹ and the regulation of fatty acid synthesis⁷⁰. Within NECSO, mitochondria function as an “energy battery”, the energy they produce being pivotal for sustaining the operation of the Na/K-ATPase and the integrity of cation gradients. In line with this, NECSO displays a distinctive characteristic: energy failure occurs prior to the rupture of the cell membrane.

In summary, we have elucidated that Na⁺ can act as an active regulator of energy metabolism, inducing cell death through the inhibition of mitochondrial energy production, thereby moving beyond the conventional osmolarity-based perspective of Na⁺-induced necrosis. We have also implicated Na/K-ATPase and AQP4 as downstream orchestrators in this process. Additionally, our work establishes a clear link between TRPM4 activation and Na⁺ overload-induced mitochondrial dysfunction, demonstrating the essential role of mitochondrial NCLX in this process. This sheds light on the potential regulatory roles of the TRPM4-NCLX axis in pathological conditions characterized by elevated cytoplasmic sodium levels, an area that warrants further investigation.

Methods

Cell culture

MCF7 and MB468 cells were cultured in Sigma Aldrich’s DMEM, supplemented with 4.5 g/L glucose, L-glutamine, 10% Gibco FBS, and 1% penicillin–streptomycin. The cells were incubated at 37 °C in a 5% CO₂ humidified environment. Routine mycoplasma testing ensured the cell line was uncontaminated.

The Na⁺-containing medium formulation is as follows: 150 mM NaCl, 5 mM KCl, 10 mM Glucose, 2 mM CaCl₂, 1 mM MgCl₂, and 10 mM HEPES. In Na⁺-free medium, NaCl is replaced with an equimolar concentration of NMDG-Cl, while all other components remain unchanged.

Gene editing

The knockout of *TRPM4* was achieved using CRISPR gene editing technology. CRISPR sgRNAs targeting *TRPM4* were designed with the online tool from the Zhang lab (<http://crispr.mit.edu/>). The oligo sequence is 5'-CCTAGGGCTCGTTCCTGCG-3'.

Seahorse assays

Real-time monitoring of the oxygen consumption rate (OCR) was executed with the employment of an XF-96 Extracellular Flux Analyzer (102416-100, Agilent). MCF7 cells were seeded into XF-96 cell culture microplates (Agilent) at a density of 8000 cells per well one day in advance to allow for overnight adhesion and attachment. After the treatment with NCI, cells were rinsed with Seahorse XF DMEM (Agilent), which had been added with 10 mM glucose (Agilent), 1 mM sodium pyruvate, and 2 mM L-glutamine (Agilent). Then, the cells were placed in an incubator at 37 °C without CO₂ for 30–60 min. A mitochondrial stress test, involving 4 cycles of 3-min mixing and subsequent 3-min OCR measurements per phase, was employed. This protocol quantified basal OCR and the cellular response to 1.5 μ M oligomycin (Agilent), 2 μ M FCCP (Agilent), and 0.5 μ M Rotenone/Antimycin A (Agilent).

For quantifying cellular ATP production rates, we introduced a real-time ATP rate assay. This involved concurrent measurements of extracellular acidification rate (ECAR) and OCR under baseline conditions and post-exposure to 1.5 μ M oligomycin and 0.5 μ M Rotenone/Antimycin A (all from Agilent). The measurements obtained were converted into ATP production rates.

After both assays, nuclear staining with Hoechst (B2261, Sigma) was required. The cell number was determined by microscopic observation to normalize the OCR readings within each well.

Determination of intracellular ATP

Intracellular ATP levels were determined using the CTG Luminafescent Assay Kit (G7570, Promega). Following the addition of 10 μ l of the reagent to each well of the 96-well plate, plates were gently shaken for 10 min to facilitate cell lysis. Subsequently, luminescence signals, indicative of ATP levels, were read using the ATPlite Luminescence Assay System (Perkin Elmer).

Cell death assays

In the LDH release assay, the culture supernatant was mixed with the LDH assay solution (CK12, Dojindo) and incubated at room temperature for 30 min. Afterward, a stop solution was added, and the absorbance was read at 490 nm on a microplate reader. A standard curve, created from a series of dilutions of the LDH control samples, was used to determine the percentage of LDH released from the treated cells. In PI staining, cells were incubated with 2 μ g/ml PI for 15 min, then observed under a microscope. The percentage of PI-positive cells was quantified using ImageJ software.

Mitochondrial membrane potential measurements

Live cell imaging: Cells cultured in four-well Lab-Tek II Chambered Cover glass imaging chambers (Thermo Fisher Scientific) were pre-loaded with 300 nM TMRE (T669, Thermo Fisher Scientific) for 30 min and subsequently rinsed with PBS twice. Then, the cells were positioned in FluoroBrite™ DMEM medium (A1896701, Thermo Fisher

Scientific) and observed under the microscope. After identifying the desired field of view, NCI was added, and imaging commenced. Fluorescence and differential interference contrast (DIC) images were captured every 5 min using a Multipoint Confocal Live Cell Imaging System (Nikon). The acquired images were analyzed using NIS Elements (Nikon) and ImageJ (NIH) software.

Flow cytometry: Cells cultured in 12-well plates, stained with 500 nM TMRE and treated with NCI, were detached with Accutase, collected in 4% FBS-PBS. TMRE fluorescence (Ex/Em = 549/575 nm) was quantified by flow cytometry.

Mitotracker analysis

MCF7 cells were seeded overnight in four-well Lab-Tek II Chambered Coverglass imaging chambers (Thermo Fisher Scientific). For mitochondrial labeling, cells were incubated with MitoTracker Red (M7512, Invitrogen) and nuclear dye Hoechst 33342 for 30 min at 37 °C. Then the cells were washed and incubated in either Na⁺-containing or Na⁺-free EBS. Thereafter, 100 nM NCI was added for the indicated time points. Fluorescence signals at each time point were captured using a confocal microscope (Olympus).

Mitochondrial calcium imaging

Live cell imaging: MCF7 cells cultured in four-well Lab-Tek II Chambered Cover glass imaging chambers (Thermo Fisher Scientific) were pre-transfected with CMV-mito-R-GECO1 (Addgene plasmid # 46021) for 24 h. Following transfection, cells were washed and then incubated in either Na⁺-containing or Na⁺-free EBS. Subsequently, cells were treated with 100 nM NCI in the respective EBS conditions. Fluorescence and differential interference contrast (DIC) images were captured every 2 min by a Multipoint Confocal Live Cell Imaging System (Nikon).

Confocal imaging: MCF7 cells were cultured in 4-well Lab-Tek II Chambered Coverglass imaging chambers (Thermo Fisher Scientific). Prior to imaging, cells were preloaded with 2 μM Rhod-2 AM (R1244, Thermo Fisher Scientific), 200 nM MitoTracker Green (M7514, Thermo Fisher Scientific), and the nuclear dye Hoechst 33342 for 30 min at 37 °C under 5% CO₂ in the dark. Following incubation, the cells were washed with either Na⁺-containing or Na⁺-free EBS and then maintained in the respective buffer conditions. NCI was subsequently added, and fluorescence signals were captured at defined time points using a confocal microscope (Olympus).

Flow cytometry: Cells cultured in 12-well plates were stained with 2 μM Rhod-2, AM, and then treated with NCI. The cells were detached using Accutase (A1110501, Thermo Fisher Scientific) and collected in PBS containing 4% FBS. Rhod-2 fluorescence (Ex/Em = 549/575 nm) was quantified by flow cytometry. In certain experiments, cells were pre-treated with 20 mM CGP-37157 (T14941, Targetmol).

Cytosolic sodium imaging

Cells grown on a glass-bottom dish were stained with 5 μM CoroNa Green, AM (c36676, Thermo Fisher Scientific) for 30 min and then treated with NCI as indicated. CoroNa Green fluorescence (Ex/Em = 492/516 nm) was observed under a confocal microscope (Olympus). The images were analyzed using ImageJ.

Electron transport chain complex assays

To assess the activity of Complex II, we utilized the Complex II Enzyme Activity Microplate Assay Kit (ab109908, Abcam). After the treatment of NCI, protein extraction of MCF7 cells was performed with a detergent solution, adjusted to the optimal concentration for assay loading. Samples were then loaded into a 96-well plate pre-coated with anti-Complex II monoclonal antibody, followed by a 2-h incubation at room temperature. After the washing step, an activity solution control buffer was added to the appropriate wells of the plate. Optical density

readings at 600 nm were taken over 60 min in kinetic mode, with 30-s interval measurements, using a Microplate Reader (Perkin Elmer).

The MitoTox Complex II+III OXPHOS Activity Assay Kit (ab109905, Abcam) was used to evaluate Complex II/III activity. Activity solution was combined with a range of NaCl concentrations (from +64 mM down to +0.0625 mM via serial dilutions). Following the addition of bovine heart mitochondria, kinetic absorbance readings at 550 nm were taken using a Microplate Reader (Perkin Elmer). Complex II/III activity levels were normalized against a solvent-only control. In certain experiments, 20 mM CGP-37157 was included.

Metabolite extraction and quantification

After NCI treatment, two million MCF7 cells were washed twice with ice-cold saline, lysed with 1 ml ice-cold 80% methanol in water, and quickly scraped into Eppendorf tubes and centrifuged at 15,000 × g for 15 min at 4 °C. The supernatant containing the soluble metabolic compounds was dried, reconstituted in 50 μl LC-MS grade water with 0.03% formic acid, vortexed, and centrifuged again. Clear supernatants were transferred to HPLC vials for subsequent LC-MS/MS analysis.

Samples were randomized and blinded before being analyzed by LC-MS/MS. Chromatographic separation was achieved on an ACQUITY UPLC HSS T3 column (2.1 × 150 mm, 1.8 μm) using an ACQUITY UPLC I-Class system (Waters Corporation, Milford, MA, USA). The mobile phases employed were 0.03% formic acid in water (A) and 0.03% formic acid in acetonitrile (B) and the gradient program was as follows: 0–3 min, 1% B; 3–15 min, 1%–99% B; 15–17 min, 99% B; 17–17.1 min, 99%–1% B; 17.1–20 min, 1% B. The flow rate was 0.25 ml min⁻¹, the column was at 35 °C, and the samples in the auto-sampler were at 4 °C. Mass spectrometry was performed using an AB QTRAP 6500+ triple quadrupole mass spectrometer (Applied Biosystems SCIEX) in multiple reaction monitoring (MRM) mode. Chromatogram review and peak area integration were performed using MultiQuant 3.0.2 (Applied Biosystems SCIEX), and the peak area of each detected metabolite was normalized to the sum of peak areas of all detected metabolites in that sample to correct for any variations introduced by sample handling through instrument analysis. The normalized data were used as variables for the multivariate and univariate statistical analysis. The analysis of enriched pathways associated with the differential metabolites was performed using Metaboanalyst v.6.0 (<https://www.metaboanalyst.ca/>). Univariate statistical differences of the metabolites between the two groups were analyzed using a two-tailed Student's *t*-test.

Mitochondrial Na⁺ detection

Mitochondria were isolated according to the mitochondrial isolation kit's (89874, Thermo Fisher Scientific) instructions and suspended in 100 μl HBSS. Samples were split evenly; one portion was incubated with 7.5 μM SBFI (MX4509, MKbio) for 45 min, while the other was used for protein quantification via BCA. SBFI fluorescence (Excitation: 340/380 nm; Emission: 520 nm) was measured on a Microplate Reader (Perkin Elmer), calculating the F340/F380 ratio as a proxy for [Na⁺], corrected by protein concentration.

Transmission electron microscopy

Transmission electron microscopy (TEM) analysis followed standard protocols: MCF7 cells treated with 100 nM NCI at various time points were fixed in 2% paraformaldehyde, 3% glutaraldehyde, and 0.1 M cacodylate buffer (pH 7.3), washed, and treated with 0.1% tannic acid. Post-fixed with 1% osmium tetroxide, cells were stained with 1% uranyl acetate, dehydrated with graded Epon, and embedded. Ultrathin sections, cut on a Leica EM UC7, were mounted on formvar-coated grids, stained with 3% uranyl acetate and lead citrate, and examined under an 80 kV TEM (H-7650, HITACHI).

Inductively coupled plasma-mass spectrometry (ICP-MS)

Samples were weighed into 50 ml metal-free tubes. 2 ml of 69% nitric acid was added, and tubes were placed on a digestion block (DigiPREP Jr., SCP-Science). Heated to 120 °C for 1 h with gentle swirling, then cooled before adding 0.5 ml H₂O₂. After reheating at 120 °C for 30 min, tubes were cooled, volumes adjusted to 20 ml with ultrapure water. Calibration standards were made by diluting 1000 mg/L ICP-MS standard solutions (Spex CertiPrep) with 10% nitric acid. Elements detected by ICP-MS (NexION2000G, PerkinElmer) using external calibration and 103Rh as an internal standard. Quality control used a certified liver reference (T07243QC, FAPAS).

In vitro Na/K-ATPase activity assay

MCF7 cells were plated at a density of 4×10^6 cells per 10 cm² dish and allowed to adhere overnight. Following adhesion, cells were treated with 50 nM NCI at the indicated time points. Then, cells were harvested using ice-cold homogenizing buffer consisting of 50 mM HEPES (pH 7.4), 250 mM sucrose, 1 mM EGTA, and a protease inhibitor cocktail. Protein extraction was achieved via Dounce homogenization with 35 strokes, followed by a low-speed centrifugation (3000 × *g* for 10 min at 4 °C). The supernatant was collected and subjected to ultracentrifugation (100,000 × *g* for 30 min at 4 °C). The resulting pellet was resuspended in 50 μl of homogenizing buffer and assayed for ATPase activity in a reaction mixture containing 50 mM HEPES (pH 7.4), 50 mM NaCl, 25 mM KCl, 5 mM MgCl₂, and 5 mM ATP, including or excluding 2 mM ouabain at 37 °C for 30 min while shaking. The enzymatic reaction was terminated by the addition of 10% trichloroacetic acid (T0699, Sigma), and samples were centrifuged to eliminate any precipitated debris (15,000 × *g*, 5 min). Enzyme activity was quantified by measuring the inorganic phosphate ([Pi]) released, using an Amalchite assay kit (MAK307, Sigma), while the protein concentration was measured using a BCA assay kit (23225, Thermo Fisher Scientific). To determine Na/K-ATPase (ouabain-sensitive) activity, the equation $([Pi] \text{ without Ouabain} - [Pi] \text{ with ouabain}) / \text{quantity of protein}$ was utilized. Experimental data are presented as relative enzyme activity (mean ± SD from three independent experiments).

Western blotting

Protein extracts from cells were prepared in RIPA buffer with a protease and phosphatase inhibitor cocktail (K1007, Apexbio), quantified using a BCA assay. Proteins (20 μg) were separated by 10% SDS-PAGE, blotted onto PVDF membranes, and blocked with 5% milk. Membranes were incubated overnight with primary antibodies, then incubated with HRP-conjugated secondary antibodies. Chemiluminescence was used for detection. The following primary antibodies were used: anti-α-tubulin (66031-1-Ig, Proteintech, diluted 1:10,000), anti-TRPM4 (A10146, Abclonal, diluted 1:1000), anti-AQP4 (A2887, Abclonal, diluted 1:1000), anti-MCU (A22525, Abclonal, diluted 1:500), and anti-Phospho-PDHA1-S293 (AP1022, Abclonal, diluted 1:1000).

siRNA transfection

The following siRNA sequences were used to knock down MCU: 1#:5'-GGGAAUUGACAGAGUUGCUTT-3', 2#:5'-CGACCUAGAGAAUACAAUTT-3'.

The siRNA sequences used to knock down AQP4 were as follows: 1#:5'-GAGCAGAAUCCUCUAUCUTT-3', 2#:5'-CACUGGCUCAAUAGCUUUATT-3'.

All siRNAs were synthesized by Shanghai GenePharma Co. Ltd. MCF7 cells were transfected with siRNA using Lipofectamine RNAiMAX (Invitrogen) following the manufacturer's protocol, and knockdown efficiency was verified by western blot.

Flow cytometry

MCF7 cells grown in 12-well plates were stained with fluorescent probes and subsequently treated with NCI. The Cells were detached

using Accutase and collected in 4% FBS-PBS. The fluorescence of stained cells was analyzed by a CytoFlex S flow cytometer (Beckman Coulter), with data processed using FlowJo.

Statistics and reproducibility

All experiments were independently replicated more than two times with consistent results. All microscopic, biochemical, and biological assays were independently repeated at least three times. GraphPad Prism 9.0 was used for statistics. Unpaired or paired two-tailed Student's *t*-test was used when comparing data from two groups. Statistical analysis for multiple group comparisons was conducted using one-way ANOVA or two-way ANOVA followed by Tukey's post hoc test. Data are presented as mean ± s.d. and *p* < 0.05 was considered statistically significant. Adobe Illustrator was used for illustrations.

Reporting summary

Further information on research design is available in the Nature Portfolio Reporting Summary linked to this article.

Data availability

All data are available within the main text or supplementary materials. Additionally, all specific and stable reagents generated during this study can be obtained from the corresponding author without any restrictions. Source data are provided with this paper.

References

1. Strazzullo, P. & Leclercq, C. Sodium. *Adv. Nutr.* **5**, 188–190 (2014).
2. Drew, D. & Boudker, O. Ion and lipid orchestration of secondary active transport. *Nature* **626**, 963–974 (2024).
3. Damkjær, M. et al. Renal renin secretion as regulator of body fluid homeostasis. *Pflug. Arch.* **465**, 153–165 (2013).
4. Marinelli, F. et al. Sodium recognition by the Na⁺/Ca²⁺ exchanger in the outward-facing conformation. *Proc. Natl. Acad. Sci. USA* **111**, E5354–E5362 (2014).
5. Zhang, M. et al. TRP (transient receptor potential) ion channel family: structures, biological functions and therapeutic interventions for diseases. *Signal Transduct. Target Ther.* **8**, 261 (2023).
6. Nguyen, P. T. et al. Structural basis for gating mechanism of the human sodium–potassium pump. *Nat. Commun.* **13**, 5293 (2022).
7. Johar, K., Priya, A. & Wong-Riley, M. T. Regulation of Na⁽⁺⁾/K⁽⁺⁾-ATPase by neuron-specific transcription factor Sp4: implication in the tight coupling of energy production, neuronal activity and energy consumption in neurons. *Eur. J. Neurosci.* **39**, 566–578 (2014).
8. Xia, B. et al. MLKL forms cation channels. *Cell Res.* **26**, 517–528 (2016).
9. Su, L. et al. A plug release mechanism for membrane permeation by MLKL. *Structure* **22**, 1489–1500 (2014).
10. Ding, J. et al. Pore-forming activity and structural autoinhibition of the gasdermin family. *Nature* **535**, 111–116 (2016).
11. Liu, X. et al. Inflammasome-activated gasdermin D causes pyroptosis by forming membrane pores. *Nature* **535**, 153–158 (2016).
12. Hirata, Y. et al. Lipid peroxidation increases membrane tension, Piezo1 gating, and cation permeability to execute ferroptosis. *Curr. Biol.* **33**, 1282–1294.e1285 (2023).
13. Hernansanz-Agustín, P. et al. Na⁺ controls hypoxic signalling by the mitochondrial respiratory chain. *Nature* **586**, 287–291 (2020).
14. Jung, D. W., Apel, L. M. & Brierley, G. P. Transmembrane gradients of free Na⁺ in isolated heart mitochondria estimated using a fluorescent probe. *Am. J. Physiol.* **262**, C1047–C1055 (1992).
15. Donoso, P., Mill, J. G., O'Neill, S. C. & Eisner, D. A. Fluorescence measurements of cytoplasmic and mitochondrial sodium concentration in rat ventricular myocytes. *J. Physiol.* **448**, 493–509 (1992).

16. Palty, R. et al. NCLX is an essential component of mitochondrial Na⁺/Ca²⁺ exchange. *Proc. Natl. Acad. Sci. USA* **107**, 436–441 (2010).
17. Tanonaka, K. et al. Possible pathway of Na⁺ flux into mitochondria in ischemic heart. *Biol. Pharm. Bull.* **35**, 1661–1668 (2012).
18. Zhang, J. et al. Necrocid 1 mediates necrotic cell death and immunogenic response in human cancer cells. *Cell Death Dis.* **14**, 238 (2023).
19. Fu, W. et al. Persistent activation of TRPM4 triggers necrotic cell death characterized by sodium overload. *Nat. Chem. Biol.* **21**, 238–1249 (2025).
20. Marshall, R. P., Droste, J. N., Giessing, J. & Kreider, R. B. Role of creatine supplementation in conditions involving mitochondrial dysfunction: a narrative review. *Nutrients* **14**, 14030529 (2022).
21. Solmonson, A. & DeBerardinis, R. J. Lipoic acid metabolism and mitochondrial redox regulation. *J. Biol. Chem.* **293**, 7522–7530 (2018).
22. Kaasik, A., Safiulina, D., Zharkovsky, A. & Veksler, V. Regulation of mitochondrial matrix volume. *Am. J. Physiol. Cell Physiol.* **292**, C157–C163 (2007).
23. González, C. et al. K⁺ channels: function-structural overview. *Compr. Physiol.* **2**, 2087–2149 (2012).
24. Geisberger, S. et al. Salt transiently inhibits mitochondrial energetics in mononuclear phagocytes. *Circulation* **144**, 144–158 (2021).
25. Côte-Real, B. F. et al. Sodium perturbs mitochondrial respiration and induces dysfunctional Tregs. *Cell Metab.* **35**, 299–315.e298 (2023).
26. Bustamante, E. & Pedersen, P. L. High aerobic glycolysis of rat hepatoma cells in culture: role of mitochondrial hexokinase. *Proc. Natl. Acad. Sci. USA* **74**, 3735–3739 (1977).
27. Rossignol, R. et al. Energy substrate modulates mitochondrial structure and oxidative capacity in cancer cells. *Cancer Res.* **64**, 985–993 (2004).
28. Weinberg, F. et al. Mitochondrial metabolism and ROS generation are essential for Kras-mediated tumorigenicity. *Proc. Natl. Acad. Sci. USA* **107**, 8788–8793 (2010).
29. Denton, R. M., Randle, P. J. & Martin, B. R. Stimulation by calcium ions of pyruvate dehydrogenase phosphate phosphatase. *Biochem. J.* **128**, 161–163 (1972).
30. Denton, R. M., Richards, D. A. & Chin, J. G. Calcium ions and the regulation of NAD⁺-linked isocitrate dehydrogenase from the mitochondria of rat heart and other tissues. *Biochem. J.* **176**, 899–906 (1978).
31. McCormack, J. G. & Denton, R. M. The effects of calcium ions and adenine nucleotides on the activity of pig heart 2-oxoglutarate dehydrogenase complex. *Biochem. J.* **180**, 533–544 (1979).
32. Prajapati, S., Rabe von Papenheim, F. & Tittmann, K. Frontiers in the enzymology of thiamin diphosphate-dependent enzymes. *Curr. Opin. Struct. Biol.* **76**, 102441 (2022).
33. Fan, J. et al. Tyr-301 phosphorylation inhibits pyruvate dehydrogenase by blocking substrate binding and promotes the Warburg effect. *J. Biol. Chem.* **289**, 26533–26541 (2014).
34. Bezawork-Geleta, A., Rohlena, J., Dong, L., Pacak, K. & Neuzil, J. Mitochondrial Complex II: at the crossroads. *Trends Biochem. Sci.* **42**, 312–325 (2017).
35. Cox, D. A., Conforti, L., Sperelakis, N. & Matlib, M. A. Selectivity of inhibition of Na⁺-Ca²⁺ exchange of heart mitochondria by benzothiazepine CGP-37157. *J. Cardiovasc. Pharm.* **21**, 595–599 (1993).
36. Van Emous, J. G., Vleggeert-Lankamp, C. L., Nederhoff, M. G., Ruijgrok, T. J. & Van Echteld, C. J. Postischemic Na⁺-K⁺-ATPase reactivation is delayed in the absence of glycolytic ATP in isolated rat hearts. *Am. J. Physiol. Heart Circ. Physiol.* **280**, H2189–H2195 (2001).
37. Sandtner, W. et al. Ouabain binding site in a functioning Na⁺/K⁺ ATPase. *J. Biol. Chem.* **286**, 38177–38183 (2011).
38. Fink, S. L. & Cookson, B. T. Caspase-1-dependent pore formation during pyroptosis leads to osmotic lysis of infected host macrophages. *Cell. Microbiol.* **8**, 1812–1825 (2006).
39. Ros, U. et al. Necroptosis execution is mediated by plasma membrane nanopores independent of calcium. *Cell Rep.* **19**, 175–187 (2017).
40. Stokum, J. A. et al. SUR1-TRPM4 and AQP4 form a heteromultimeric complex that amplifies ion/water osmotic coupling and drives astrocyte swelling. *Glia* **66**, 108–125 (2018).
41. Xie, N. et al. NAD⁺ metabolism: pathophysiologic mechanisms and therapeutic potential. *Signal Transduct. Target Ther.* **5**, 227 (2020).
42. Wescott, A. P., Kao, J. P. Y., Lederer, W. J. & Boyman, L. Voltage-energized calcium-sensitive ATP production by mitochondria. *Nat. Metab.* **1**, 975–984 (2019).
43. Jouaville, L. S., Pinton, P., Bastianutto, C., Rutter, G. A. & Rizzuto, R. Regulation of mitochondrial ATP synthesis by calcium: evidence for a long-term metabolic priming. *Proc. Natl. Acad. Sci. USA* **96**, 13807–13812 (1999).
44. Carraro, M. & Bernardi, P. The mitochondrial permeability transition pore in Ca²⁺ homeostasis. *Cell Calcium* **111**, 102719 (2023).
45. Calvo-Rodríguez, M. et al. Increased mitochondrial calcium levels associated with neuronal death in a mouse model of Alzheimer’s disease. *Nat. Commun.* **11**, 2146 (2020).
46. Orrenius, S., Zhivotovsky, B. & Nicotera, P. Regulation of cell death: the calcium-apoptosis link. *Nat. Rev. Mol. Cell Biol.* **4**, 552–565 (2003).
47. Kirichok, Y., Krapivinsky, G. & Clapham, D. E. The mitochondrial calcium uniporter is a highly selective ion channel. *Nature* **427**, 360–364 (2004).
48. Luongo, T. S. et al. The mitochondrial Na⁺/Ca²⁺ exchanger is essential for Ca²⁺ homeostasis and viability. *Nature* **545**, 93–97 (2017).
49. Scambler, T. et al. ENaC-mediated sodium influx exacerbates NLRP3-dependent inflammation in cystic fibrosis. *Elife* **8**, 49248 (2019).
50. Shrivastava, A. N. et al. α-synuclein assemblies sequester neuronal α3-Na⁺/K⁺-ATPase and impair Na⁺ gradient. *EMBO J.* **34**, 2408–2423 (2015).
51. Carrithers, M. D. et al. Regulation of podosome formation in macrophages by a splice variant of the sodium channel SCN8A. *J. Biol. Chem.* **284**, 8114–8126 (2009).
52. Wang, J. et al. Hepatitis B virus-mediated sodium influx contributes to hepatic inflammation via synergism with intrahepatic danger signals. *iScience* **27**, 108723 (2024).
53. Mutchler, S. M., Kirabo, A. & Kleyman, T. R. Epithelial sodium channel and salt-sensitive hypertension. *Hypertension* **77**, 759–767 (2021).
54. Iwai, T. et al. Sodium accumulation during ischemia induces mitochondrial damage in perfused rat hearts. *Cardiovasc. Res.* **55**, 141–149 (2002).
55. Daniele, S. G. et al. Brain vulnerability and viability after ischaemia. *Nat. Rev. Neurosci.* **22**, 553–572 (2021).
56. Pogwizd, S. M., Sipido, K. R., Verdonck, F. & Bers, D. M. Intracellular Na in animal models of hypertrophy and heart failure: contractile function and arrhythmogenesis. *Cardiovasc. Res.* **57**, 887–896 (2003).
57. Aksentijević, D. et al. Intracellular sodium elevation reprograms cardiac metabolism. *Nat. Commun.* **11**, 4337 (2020).
58. Liu, T. et al. Inhibiting mitochondrial Na⁺/Ca²⁺ exchange prevents sudden death in a Guinea pig model of heart failure. *Circ. Res.* **115**, 44–54 (2014).
59. Martínez-Sanz, F. J. et al. Neuroprotective profile of pyridothiazepines with blocking activity of the mitochondrial Na⁺/Ca²⁺ exchanger. *Eur. J. Med. Chem.* **109**, 114–123 (2016).

60. Jadiya, P. et al. Impaired mitochondrial calcium efflux contributes to disease progression in models of Alzheimer's disease. *Nat. Commun.* **10**, 3885 (2019).
61. Hagenston, A. M. et al. Disrupted expression of mitochondrial NCLX sensitizes neuroglial networks to excitotoxic stimuli and renders synaptic activity toxic. *J. Biol. Chem.* **298**, 101508 (2022).
62. Jornot, L., Maechler, P., Wollheim, C. B. & Junod, A. F. Reactive oxygen metabolites increase mitochondrial calcium in endothelial cells: implication of the $\text{Ca}^{2+}/\text{Na}^{+}$ exchanger. *J. Cell Sci.* **112**, 1013–1022 (1999).
63. Czyz, A. & Kiedrowski, L. Inhibition of plasmalemmal $\text{Na}^{+}/\text{Ca}^{2+}$ exchange by mitochondrial $\text{Na}^{+}/\text{Ca}^{2+}$ exchange inhibitor 7-chloro-5-(2-chlorophenyl)-1,5-dihydro-4,1-benzothiazepin-2(3H)-one (CGP-37157) in cerebellar granule cells. *Biochem. Pharm.* **66**, 2409–2411 (2003).
64. Ruiz, A., Alberdi, E. & Matute, C. CGP37157, an inhibitor of the mitochondrial $\text{Na}^{+}/\text{Ca}^{2+}$ exchanger, protects neurons from excitotoxicity by blocking voltage-gated Ca^{2+} channels. *Cell Death Dis.* **5**, e1156 (2014).
65. Viejo, L. et al. Synthesis and biological assessment of 4,1-benzothiazepines with neuroprotective activity on the Ca^{2+} overload for the treatment of neurodegenerative diseases and stroke. *Molecules* **26**, 26154473 (2021).
66. Goldstein, J. C., Waterhouse, N. J., Juin, P., Evan, G. I. & Green, D. R. The coordinate release of cytochrome c during apoptosis is rapid, complete and kinetically invariant. *Nat. Cell Biol.* **2**, 156–162 (2000).
67. Hegde, R. et al. Identification of Omi/HtrA2 as a mitochondrial apoptotic serine protease that disrupts inhibitor of apoptosis protein–caspase interaction. *J. Biol. Chem.* **277**, 432–438 (2002).
68. Du, C., Fang, M., Li, Y., Li, L. & Wang, X. Smac, a mitochondrial protein that promotes cytochrome c-dependent caspase activation by eliminating IAP inhibition. *Cell* **102**, 33–42 (2000).
69. Murphy, M. P. How mitochondria produce reactive oxygen species. *Biochem. J.* **417**, 1–13 (2009).
70. Gao, M. et al. Role of mitochondria in ferroptosis. *Mol. Cell* **73**, 354–363.e353 (2019).

Acknowledgements

The work was supported in part by grants from the Ministry of Science and Technology of the People's Republic of China (MOST) (2023YFA0914900), National Natural Science Foundation of China (NSFC) (92254307, 32361163613, M-0140, 82504119), Shanghai Municipal Health Commission (2024ZZ1031), and the Fundamental Research Funds for the Central Universities to Q.Z.; The work was also supported by an innovative research team of high-level local universities in Shanghai (SHSMU-ZDCX20212000), Shanghai Science and Technology Commission (25ZR1402292) and Shanghai Frontiers Science Center of Cellular Homeostasis and Human Diseases to Q.Z.

Author contributions

Y.Q. started the project and performed most of the experiments with the help of J.W., H.Z., and W.F. B.W. and Q.N. contributed with metabolomics, with guidance from Z.H. Y.Q. and Q.Z. conceived the project, designed the experiments, analyzed the data, and wrote the manuscript, with contributions from all authors. All authors discussed the results and commented on the manuscript.

Competing interests

The authors declare no competing interests.

Additional information

Supplementary information The online version contains supplementary material available at <https://doi.org/10.1038/s41467-025-67181-x>.

Correspondence and requests for materials should be addressed to Wan Fu, Zeping Hu or Qing Zhong.

Peer review information *Nature Communications* thanks John Elrod and the other anonymous reviewer(s) for their contribution to the peer review of this work. A peer review file is available.

Reprints and permissions information is available at <http://www.nature.com/reprints>

Publisher's note Springer Nature remains neutral with regard to jurisdictional claims in published maps and institutional affiliations.

Open Access This article is licensed under a Creative Commons Attribution-NonCommercial-NoDerivatives 4.0 International License, which permits any non-commercial use, sharing, distribution and reproduction in any medium or format, as long as you give appropriate credit to the original author(s) and the source, provide a link to the Creative Commons licence, and indicate if you modified the licensed material. You do not have permission under this licence to share adapted material derived from this article or parts of it. The images or other third party material in this article are included in the article's Creative Commons licence, unless indicated otherwise in a credit line to the material. If material is not included in the article's Creative Commons licence and your intended use is not permitted by statutory regulation or exceeds the permitted use, you will need to obtain permission directly from the copyright holder. To view a copy of this licence, visit <http://creativecommons.org/licenses/by-nc-nd/4.0/>.

© The Author(s) 2025